Inorganic Chemistry

pubs.acs.org/IC

Article

Multistimuli-Responsive Properties of Aggregated Isocyanide Cycloplatinated(II) Complexes

Mónica Martínez-Junquera, Elena Lalinde,* and M. Teresa Moreno*

Cite This: *Inorg. Chem.* 2022, 61, 10898−10914

Read Online

ACCESS | Metrics & More | Article Recommendations | Supporting Information

ABSTRACT: Here, we describe the neutral cyclometalated *tert*-butylisocyanide Pt^{II} complexes, $[Pt(C^N)Cl(CNBu^t)]$ **1**, the double salts $[Pt(C^N)(CNBu^t)_2][Pt(C^N)Cl_2]$ **2**, and the cationic complexes $[Pt(C^N)(CNBu^t)_2]ClO_4$ **3** [C∧N = difluorophenylpyridine (dfppy, **a**), 4-(2-pyridyl)benzaldehyde (ppy-CHO, **b**)]. A comparative study of the pseudopolymorphs **1a**, **1a·CHCl$_3$**, **1b**, **1b·0.5Toluene**, **1b·0.5PhF**, and **3a·0.25CH$_2$Cl$_2$** reveals strong aggregation through Pt···Pt and/or $\pi\cdots\pi$ stacking interactions to give a variety of distinctive one-dimensional (1D) infinite chains, which modulate the photoluminescent properties. This intermolecular long-range aggregate formation is the main origin of the photoluminescent behavior of **1a** and **1b** complexes, which exhibit highly sensitive and reversible responses to multiple external stimuli including different volatile organic compounds (VOCs), solvents, temperatures, and pressures, with distinct color and phosphorescent color switching from green to red. Furthermore, complex **1b** undergoes supramolecular self-assembly *via* Pt···Pt and/or $\pi\cdots\pi$ interactions into a polymer thin polystyrene (PS) film 10 wt % in response to toluene vapors, and **3a** exhibits vapochromic and vapoluminescent behavior. Theoretical simulations on the dimer, trimer, and tetramer models of **1a** and **1b** have been carried out to get insight into the photophysical properties in the aggregated solid state.

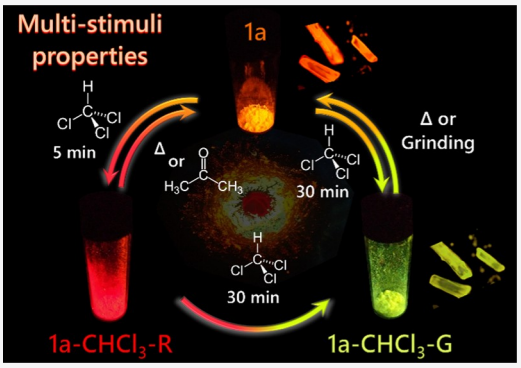

INTRODUCTION

Currently, there is a great deal of interest in producing chromic Pt^{II} complexes, with changes in the color or luminescence upon the application of external stimuli.[1] Most of the studies focus on changes in luminescence using as external stimuli liquids,[2] vapors,[3] temperature,[3d,4] or mechanical grinding[5] of interest in memory, sensors, and optoelectronics.[6] Some excellent reviews about these topics have been published.[7] Many complexes only respond to a single external stimulus, with the systems that respond to multiple external stimuli being rare.[3d,4b,8]

The versatile chromic behavior of the Pt^{II} complexes is a consequence of their rigid square planar geometry, which enables noncovalent $\pi\cdots\pi$ stacking and intra- or intermolecular Pt···Pt interactions *via* open axial positions. These interactions endow supramolecular structures generating $^3\pi\pi$ excimeric and metal−metal-to-ligand charge-transfer (^{3}MMLCT) transitions, respectively, remarkably red-shifted in comparison to the intraligand (^{3}IL), ligand−ligand charge-transfer (^{3}LLCT) or metal-to-ligand charge-transfer (^{3}MCLT) transitions present in the monomer.[7a,g,9] The interplanar and metallophilic interactions, with Pt···Pt separations shorter than the sum of van der Waals radii, can allow the formation of dimers, trimers, oligomers, or one-dimensional (1D)-stacked structures,[3a,7g,10] and some of these systems have been successfully utilized to develop white light, deep-red to near-infrared organic light-emitting diodes (OLEDs) or data storage devices.[11] However, intermolecular interactions can also cause nonradiative deactivation.[12] Considering that the metallophilic Pt···Pt interactions show a bond strength comparable to that of the hydrogen bonding,[13] these relatively weak interactions can be affected by steric effects or other noncovalent intra-/intermolecular interactions such as solvation, hydrogen/halogen interactions, etc.[7b,14] In consequence, noncovalent interactions play key roles in the assembly of platinum systems that respond to external stimuli and in the modulation of the photoluminescence properties of the resulting materials.[7a,15]

Among chromic Pt^{II} systems, a number of cyclometalated Pt^{II} complexes have been developed as a means to achieve bright, colorful luminescent materials.[1,2,7c,e,i,16] On the other hand, isocyanides are versatile synthons for photoluminescent platinum complexes, which show stimuli response properties,[17] and on some occasions, the luminescence can be modulated by noncovalent interactions.[18] In this field, some chromic cyclometalated complexes containing the strong field ligand isocyanides have been documented,[14a,19] and it has been demonstrated that their photophysical properties can be

Received: April 25, 2022
Published: July 1, 2022

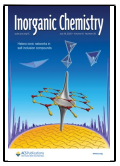

Scheme 1. Synthesis of 1−3 (a, b), (i) 1 equiv of $CNBu^t$, CH_2Cl_2; Dryness and Treatment with Toluene, (ii) Excess of $KClO_4$ and 2 equiv of $CNBu^t$, Acetone/CH_2Cl_2 (1/1), and 298 K

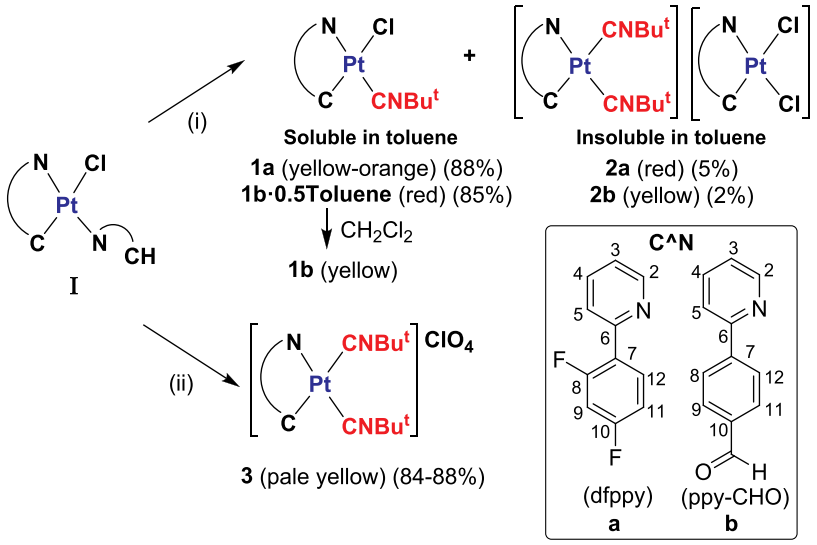

modulated effectively by adjusting steric effects, the strength of the intermolecular interactions, or the medium. In this line, our group has reported two families of chloro-cyclometalated complexes, the benzoquinolinyl [Pt(bzq)Cl(CNR)],[14a] in which isocyanide was varied, [R = *tert*-butylisocyanide (Bu^t); 2,6-dimethylphenyl (Xyl); 2-naphthyl (2-Np)], and the xylylisocyanide compounds, [Pt(C^N)Cl(CNXyl)], in which the cyclometalated backbone was modified [HC^N = 2-phenylpyridine (ppy); 2,4-difluorophenylpyridine (dfppy); and phenylquinoline (pq)],[19a] aiming to examine the role of the intermolecular $\pi\cdots\pi$ and short- or long-range Pt···Pt stacking interactions on their structural arrays and photophysical properties. The higher self-assembly behavior in the ground and excited state was found for the bzq/$CNBu^t$, 2-Np and ppy-based complexes.

In this work, we report the preparation, characterization, and optical study of cyclometalated isocyanide Pt^{II} complexes, [Pt(C^N)Cl($CNBu^t$)] **1**, the double salts [Pt(C^N)($CNBu^t$)$_2$]-[Pt(C^N)Cl_2] **2**, and the cationic complexes [Pt(C^N)-($CNBu^t$)$_2$]ClO_4 **3** with difluorophenylpyridine (dfppy, **a**) or formyl-functionalized phenylpyridine (ppy-CHO, **b**) cyclometalated ligands. Among them, we discuss in depth the relationship between the structure−optical properties of complexes that display chromism upon the application of one or several stimuli. In particular, we present the differences in the crystal packing and luminescent properties of several pseudo-polymorphs of **1a** and **1b** and the effect of solvents (vapochromism and solvatochromism), temperature (thermochromism), and mechanical force (mechanochromism), together with the vapochromism of **3a**.

SYNTHESIS AND CHARACTERIZATION OF COMPLEXES

The synthesis of the cycloplatinated chloride−isocyanide complexes [Pt(C∧N)Cl($CNBu^t$)] (**1**) and bis-isocyanide [Pt(C^N)($CNBu^t$)$_2$]ClO_4 (**3**) complexes was carried out using the corresponding complexes containing HC∧N as an auxiliary ligand as precursors, [Pt(C^N)(HC^N)Cl] (C^N = dfppy **Ia**,[20] ppy-CHO **Ib**). Precursor **Ib** was prepared in this work following a conventional protocol, which involves the reaction of K_2PtCl_4 with an excess of HC^N in an ethoxyethanol/water mixture at 80 °C.

The reaction of the corresponding precursor **Ia** or **Ib** with 1 equiv of $CNBu^t$ in CH_2Cl_2 at room temperature and further treatment of the dry residue with toluene gave a minority solid, insoluble in toluene, and a major product soluble in toluene (Scheme 1i). The main product, identified as [Pt(C^N)Cl-($CNBu^t$)], was obtained from the toluene solution in high yields (85−88%) as a yellow-orange (C^N = dfppy **1a**) or a red solvated solid (C^N = ppy-CHO **1b·0.5Toluene**). Interestingly, **1b·0.5Toluene** keeps its color in solid for more than 1 month, finally changing to a yellow solid on standing, suggesting that a structural transformation takes place. Indeed, it is also isolated as unsolvated yellow solid (**1b**) by dissolution in CH_2Cl_2 and evaporation to dryness. These complexes **1** are rather soluble in common organic solvents. Spectroscopic analysis and X-ray diffraction (XRD) of crystals of **1a** and **1b** from different solvents (see below) reveal that complexes **1** display the stereochemistry shown in Scheme 1 with $CNBu^t$ occupying the trans position to the nitrogen of the C^N ligand, similarly to other chloride−isocyanides published[14a,19a,21] and consistent with the lower trans influence of Cl^- compared to the $CNBu^t$ ligand. They exhibit one ν(Pt−Cl) absorption at 289 cm^{-1}, consistent with a terminal Pt−Cl bond trans to C, and one absorption at 2207 **1a** and 2205 cm^{-1} **1b**, assignable to ν(C≡N) of terminal $CNBu^t$, which is shifted to higher frequencies with respect to the free ligand (2125 cm^{-1}). Spectroscopically, the microcrystals obtained from different solvents exhibit almost identical ν(C≡N) bands to the pristine solids (2207−2211 **1a**, 2202−2205 cm^{-1} **1b**). Their electrospray ionization (ESI)(+)-mass spectrometry (MS) spectra show the peak corresponding to the loss of chloride ($[M - Cl]^+$) and that corresponding to the dimer $[2M - Cl]^+$, suggesting a strong tendency to form aggregates. ^1H and $^{13}C\{^1H\}$ NMR spectra of complexes **1** display the expected signals for C^N and $CNBu^t$ in a 1:1 intensity ratio, which were assigned on the basis of $^1H-^1H$ and $^{13}C-^1H$ correlations (see the Experimental Section and Figures S1 and S2). The minority solids were proposed as the double salts [Pt(C^N)($CNBu^t$)$_2$][Pt(C^N)Cl_2] (red solid, C^N = dfppy, **2a**; yellow, C^N = ppy-CHO **2b**) in agreement with their matrix-assisted laser desorption ionization time-of-flight

https://doi.org/10.1021/acs.inorgchem.2c01400
Inorg. Chem. 2022, 61, 10898−10914

Table 1. Color, Color Emission, and Selected Distances (Å) and Angles (deg) of Crystals 1a, 1a·$CHCl_3$, 1b, 1b·0.5Toluene, and 1b·0.5PhF

	1a[a]	1a·$CHCl_3$	1b	1b·0.5Toluene[a]	1b·0.5PhF[a]
color	yellow	pale-yellow	yellow	orange-red	orange-red
emission	orange	green-yellow	yellow	red	red
Pt(1)−Cl(1) (Å)	2.385(2)	2.399(12)	2.3952(8)	2.4054(9)	2.4001(9)
Pt(1)−N(1) (Å)	2.054(5)	2.054(3)	2.057(3)	2.057(3)	2.061(3)
Pt(1)−C_{ort} (Å)	1.986(3)	1.986(4)	1.992(3)	1.992(3)	1.988(4)
Pt(1)−C_{CNBu^t} (Å)	1.921(7)	1.898(4)	1.894(3)	1.913(4)	1.908(4)
Pt···Pt (Å)	$3.818_{(dimer)}$/3.688	5.305/6.541	5.337	$3.362_{(dimer)}$/3.896	$3.370_{(dimer)}$/3.864
$d_{interplanar}$ (Å)[b]	$3.448_{(dimer)}$/3.531	3.467/3.523	3.434	$3.329_{(dimer)}$/3.306	$3.298_{(dimer)}$/3.331
Pt···Pt···Pt (deg)	∼145	73.33	79.70	∼147	∼146
C_α−Pt−Pt−C_α (deg)	75.93/72.84	180.0	180.0	64.79/58.51	63.80/57.78

[a]Pair of molecules with similar distances and angles were found in the crystals of **1a**, **1b·0.5Toluene**, and **1b·0.5 PhF**. Data are given for molecule A. [b]Shortest interplanar distance.

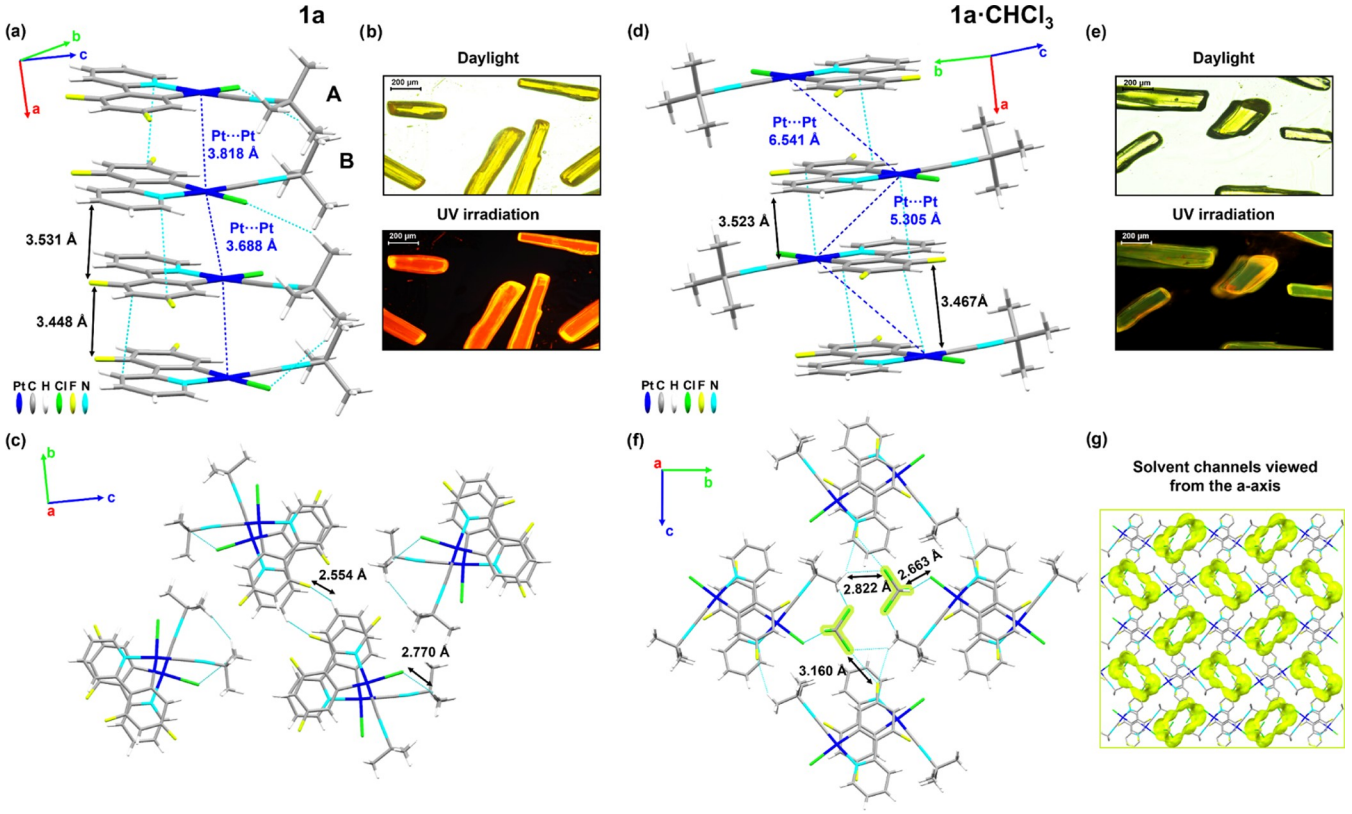

Figure 1. (a) Single infinite crystal stacking along the *a*-axis of molecules AB showing the $\pi\cdots\pi$ interplanar and Pt···Pt distances. Hydrogen atoms are omitted for clarity. (b) Pictures of crystals of **1a** under daylight or UV irradiation. (c) Top view from the *a*-axis of four stackings showing also C−H···F contacts between columns. (d) Packing structure of **1a·$CHCl_3$** along the *a*-axis showing the $\pi\cdots\pi$ interplanar and Pt···Pt distances. (e) Pictures of crystals of **1a·$CHCl_3$** under daylight or UV irradiation. (f) Axial visualization of solvent interactions along the stacking direction. (g) View of the packing structure with the solvent channels marked in yellow along the *a*-axis. This picture was illustrated using the Mercury computer program.[24]

(MALDI-TOF) spectra, which show peaks due to the corresponding anion $[Pt(C^N)Cl_2]^-$ and cation $[Pt(C^N)(CNBu^t)_2]^+$ operating in a negative and positive mode, respectively (Figures S3 and S4), and two characteristic $\nu(C{\equiv}N)$ absorptions due to the two terminal $CNBu^t$ ligands. To corroborate this proposal, red complex **2a** was obtained alternatively by a reaction of $(NBu_4)[Pt(dffpy)Cl_2]$ (generated *in situ* from $[Pt(dfppy)(\mu\text{-}Cl)]_2$ with 2 equiv of NBu_4Cl in refluxing MeOH) and complex **3a**, $[Pt(dffpy)(CNBu^t)_2]ClO_4$. Its insolubility in common organic solvents prevents the characterization by NMR spectroscopy and X-ray spectroscopy. **2a** does not show solid-state evolution by thermal treatment in an oven (100 °C) for 24 h into the corresponding neutral complex $[Pt(dfppy)Cl(CNBu^t)]$, a common feature in double salts.[14a,22] A similar reaction between $(NBu_4)[Pt(ppy\text{-}CHO)Cl_2]$ and **3b** also evolves with the formation of the expected salt **2b** but mixed with **1b** due to a relatively fast rearrangement of the salt. This type of behavior is not unusual. Indeed, the salt $[Pt(bzq)(CN\text{-}2\text{-}Np)_2][Pt(bzq)Cl_2]$ was also formed as a subproduct together with $[Pt(bzq)Cl(CN\text{-}2\text{-}Np)]$ by reacting $[Pt(bzq)(\mu\text{-}Cl)]_2$ and CN-2-Np in a 1:2 molar ratio.[14a]

Cationic complexes $[Pt(C^N)(CNBu^t)_2]ClO_4$ (C^N = dfppy **3a**, ppy-CHO **3b**) were prepared by treatment of a suspension of the corresponding $[Pt(C^N)(HC^N)Cl]$ (**Ia**, **Ib**) precursor

https://doi.org/10.1021/acs.inorgchem.2c01400
Inorg. Chem. 2022, 61, 10898−10914

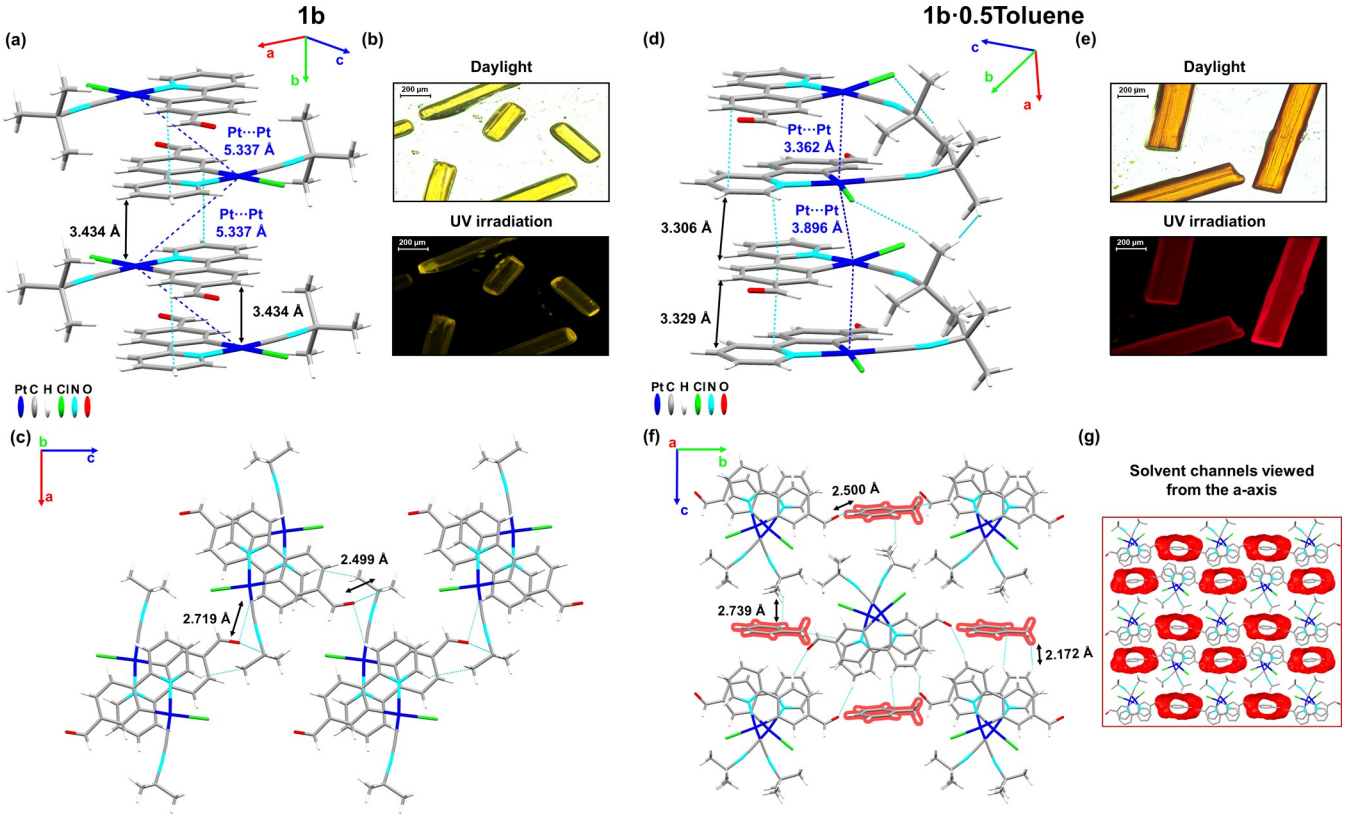

Figure 2. (a) Single infinite crystal packing of **1b** along the *a*-axis showing the $\pi\cdots\pi$ interplanar and Pt···Pt distances. (b) Pictures of crystals of **1b** under daylight or UV irradiation. (c) Top view from the *b*-axis of four columns, showing also $H_{(ppy-CHO)}\cdots O_{(ppy-CHO)}$ interactions. (d) Columnar stacking along the *a*-axis of **1b·0.5Toluene** showing the $\pi\cdots\pi$ interplanar and Pt···Pt distances. (e) Pictures of crystals of **1b·0.5Toluene** under daylight or UV irradiation. (f) Top view from the *a*-axis of five stackings showing the toluene solvent localization and secondary contacts. (g) View of the packing structure with the solvent channels marked in red along the *a*-axis.

with an excess of $KClO_4$ and the subsequent addition of 2 equiv of $CNBu^t$ in a mixture of acetone/CH_2Cl_2 (1/1) (Scheme 1ii). These complexes were isolated as pale-yellow air-stable solids in good yields (84−88%). They exhibit two terminal $\nu(C{\equiv}N)$ absorptions at 2236, 2215 **3a**, 2248, and 2223 cm^{-1} **3b**, shifted to higher energies than in **1**, and peaks at 1085 and 622−624 cm^{-1}, assigned to the ionic ClO_4^-. The ESI(+) mass spectra show the corresponding $[Pt(C^N)(CNBu^t)_2]^+$ peaks and the NMR spectra (^1H and $^{13}C\{^1H\}$) show the expected signals of C^N/$CNBu^t$ in a 1:2 intensity ratio. It is worth noting that in **3**, the most deshielded H^2 proton appears high-field shifted in relation to complexes **1** (δ H^2 8.90 **3a** *vs* 9.47 **1a**; 8.78 **3b** *vs* 9.80 **1b**) (Figures S5 and S6), as a consequence of the substitution of Cl^- by $CNBu^t$.

CRYSTALLOGRAPHIC STUDIES

For **1a**, crystals suitable for X-ray diffraction were obtained by slow diffusion of *n*-hexane into a CH_2Cl_2 solution (**1a**) or by evaporation from a concentrated $CHCl_3$ solution (**1a·CHCl$_3$**), and for **1b**, by slow diffusion at 298 K of *n*-hexane into tetrahydrofuran (THF), toluene, or fluorobenzene solutions, respectively (**1b**, **1b·0.5Toluene**, **1b·0.5PhF**), and they were subjected to single-crystal X-ray analysis. The basic crystallographic data and selected bond distances and angles are summarized in Tables 1 and S1−S3. Their structural analyses reveal the expected distorted square planar geometry with the isocyanide ligand in the trans position with respect to the nitrogen of the cyclometalated groups (Figures 1 and 2). All distances and angles are comparable to those observed in related complexes.[14a,19a,21]

Yellow needles of **1a** show orange emission similar to **1a** powder, whereas the pale-yellow crystals of **1a·CHCl$_3$** display a green-yellow emission due to their different molecular stacking (Figure 1). **1a** presents two nearly identical molecules (A and B) in the asymmetric unit (data given for A in Table 1) that form head-to-head slightly twisted parallel dimers (AB), which stack along the *a*-axis (Figure 1a), with alternating C_α−Pt−Pt−$C_{\alpha(CNBu^t)}$ angles of 75.93/72.84°, interplanar dfppy $\pi\cdots\pi$ interactions of 3.448 (dimer)/3.531 Å and Pt···Pt distances of 3.818 (dimer)/3.688 Å, close to the van der Waals limit, which is around 3.5 Å.[23] The Pt atoms in the columns are rather aligned with a Pt−Pt−Pt angle of ∼145°. Inside the columns, there are also secondary $C-H_{(Bu^t)}\cdots Cl$ interactions (2.770 Å) and the columns interact through C−H···F contacts (2.554 Å) (Figure 1c).

The **1a·CHCl$_3$** crystals also show a staggered columnar packing. The molecules stack along the *a*-axis in a head-to-tail manner with an antiparallel arrangement, which minimizes the repulsion between the *tert*-butyl moieties (C_α−Pt−Pt−C_α angle of 180°, Figure 1f), and alternating $\pi\cdots\pi$ interactions, similar to those found in **1a** (3.467 and 3.523 Å, Figure 1d and Table 1). The Pt−Pt distances are longer than in **1a** (5.305 and 6.541 Å) with a zigzag Pt−Pt−Pt angle of 73.33°. Interestingly, the molecules of the solvent are occluded in continuous channels along the *a*-axis, with two rows of $CHCl_3$ per cavity interacting with the complex [$Cl\cdots Cl/H_{(solvent)}$ 2.663 Å, $F\cdots Cl_{(solvent)}$ 3.160 Å, and $H_{(Bu^t)}\cdots Cl_{(solvent)}$ 2.822 Å] (Figures 1f,g and S7). The

https://doi.org/10.1021/acs.inorgchem.2c01400
Inorg. Chem. 2022, 61, 10898−10914

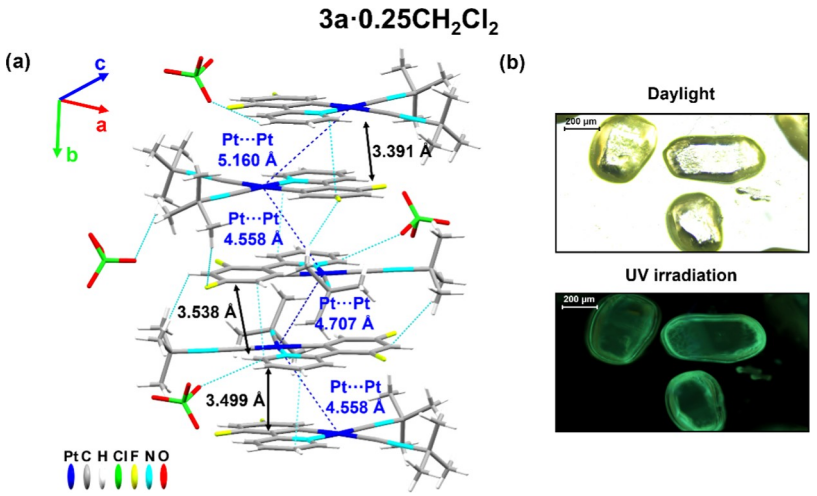

Figure 3. (a) Single infinite crystal packing of **3a·0.25CH$_2$Cl$_2$** along the *b*-axis showing the $\pi\cdots\pi$ interplanar and Pt···Pt distances. (b) Pictures of crystals of **3a·0.25CH$_2$Cl$_2$** under daylight or UV irradiation.

channels have an aperture size of 11.1 Å × 10.3 Å, and the total void volume occupies 26.3% of the unit cell. The green-yellow emission of these crystals changes to orange on standing in the air (4 h), suggesting that the $CHCl_3$ molecules are lost, reversing to **1a**. The shorter Pt−Pt distances in **1a** could account for the lower-energy emissions of the crystals of **1a** in relation to **1a·CHCl$_3$**. The vapochromic behavior of the powder **1a** (see below) could be related to the occurrence of a structural transformation from the initial framework of **1a**, in which the molecules present a head-to-head disposition to the porous channel structure of **1a·CHCl$_3$**, with the molecules adopting a head-to-tail arrangement. The solvent channels appear to be more accessible to absorb vapors of solvent molecules, thereby resulting in a rapid vapochromic response (see below).

Yellow needles of **1b** display a staggered columnar packing, which resembles **1a·CHCl$_3$** (Figure 2), with a regular antiparallel head-to-tail arrangement of neighboring molecules with $\pi\cdots\pi$ (ppy-CHO) interactions of 3.434 Å and a long Pt···Pt distance (5.337 Å), indicative of negligible metallophilic interactions. The Pt−Pt−Pt and torsional C_α−Pt−Pt−C_α angles are 79.70 and 180.0°, respectively (Figure 2a,c).

The red needles crystals of **1b·0.5Toluene** and **1b·0.5PhF** display very similar crystallographic data and structural arrangement, with small variations that fit within the experimental error (Figures 2 and S8). Therefore, only the structure of **1b·0.5Toluene** will be discussed. In **1b·0.5Toluene**, the two nearly identical molecules (A and B) found in the asymmetric unit form a head-to-head dimer with a short Pt···Pt distance of 3.362 Å and a $\pi\cdots\pi$ (ppy-CHO) interplanar distance of 3.329 Å (Figure 2d,f). The short distances[23] imply a strong Pt−Pt interaction within the dimeric unit, which could account for the lower-energy emissions of crystals **1b·0.5Toluene** at 298 K, intensified by cooling. The dimers stack along the *a*-axis to form a columnar structure with a C_α−Pt−Pt−C_α torsion angle of 64.79/58.51° and a slight zigzag Pt−Pt−Pt arrangement (angle ∼147°), thus increasing the Pt···Pt distance (3.896 Å) between dimers. These columns are mainly supported by interplanar ppy-CHO $\pi\cdots\pi$ (3.306 Å) and secondary Cl···H$_{(Bu^t)}$ (2.893 Å) interactions. A notable structural feature is the presence of a channel with an approximately 6 Å pore diameter along the *a*-axis, running parallel with the Pt···Pt stacks, partly occupied by toluene molecules in this red crystalline form, supported by weak contacts such as O$_{(ppy\text{-}CHO)}\cdots$H$_{Ph/Me(Tol)}$ (2.500 Å), H$_{(ppy\text{-}CHO/Bu)}\cdots$C$_{Me(Tol)}$ (2.739 Å), and H$_{(ppy\text{-}CHO)}\cdots$H$_{Me(Tol)}$ (2.172 Å) (Figures 2g and S9). The solvent-accessible volume occupies 22.7% of the total volume of the unit cell for **1b·0.5Toluene** and 18.1% for **1b·0.5PhF**. Different solvents were studied (THF, xylene, acetone, $CHCl_3$, and MeCN), and only red crystals were obtained from toluene and fluorobenzene. This fact suggests that the formation of channels seems to be driven by the required solvent space and the interactions between solvent molecules and the platinum moieties. These structures are stable with time, as solvent molecules are "trapped", as evidenced by the fact that the red crystal lasted more than 1 month to lose the solvent and its color into the air. Structural analysis of **1b·0.5Toluene** and **1b·0.5PhF** provides insight into the solvent exchange mechanism, enabling rationalization of the vapochromic response that will be detailed in the corresponding section (see below).

Microcrystals of **3a·0.25CH$_2$Cl$_2$** and pale-yellow blocks of **3b** were obtained by slow diffusion of *n*-hexane into a solution of the corresponding compound in CH_2Cl_2 at 298 K (Figures 3 and S10 and Table S4). For **3b**, the quality of the data collection was not good enough, and only the connectivity and the packing were established (Figure S11). Crystals of **3a·0.25CH$_2$Cl$_2$** contain four nearly identical molecules in the asymmetric unit, and only selected parameters for molecule A are given in Table S5. The cation exhibits the expected distorted square planar geometry formed by the dfppy and two *tert*-butylisocyanide ligands. In the crystal lattice, the cations form columnar structures along the *a*- and *b*-axis *via* partial π-stacking between two dfppy units from neighboring molecules, which have an antiparallel arrangement with short $\pi\cdots\pi$ interactions (3.391 Å) and a long Pt···Pt separation (5.160 Å). As shown in the Supporting Information (Figure S10), the dimers packed with other twisted units through a longer $\pi\cdots\pi$ (3.499, 3.538 Å) and a shorter Pt···Pt distance (4.558, 4.707 Å) and also show secondary C−H$_{(Bu^t)}\cdots$F$_{(dfppy)}$ (2.472 Å) and H$_{(dfppy/Bu^t)}\cdots$O$_{(ClO4)}$ (2.494−2.525 Å) contacts.

PHOTOPHYSICAL PROPERTIES AND THEORETICAL CALCULATIONS

Absorption Spectra in Solution and Density Functional Theory (DFT) Calculations. The absorption spectra of the complexes **1a**, **1b**, **3a**, and **3b** were recorded in a CH_2Cl_2

https://doi.org/10.1021/acs.inorgchem.2c01400
Inorg. Chem. 2022, 61, 10898−10914

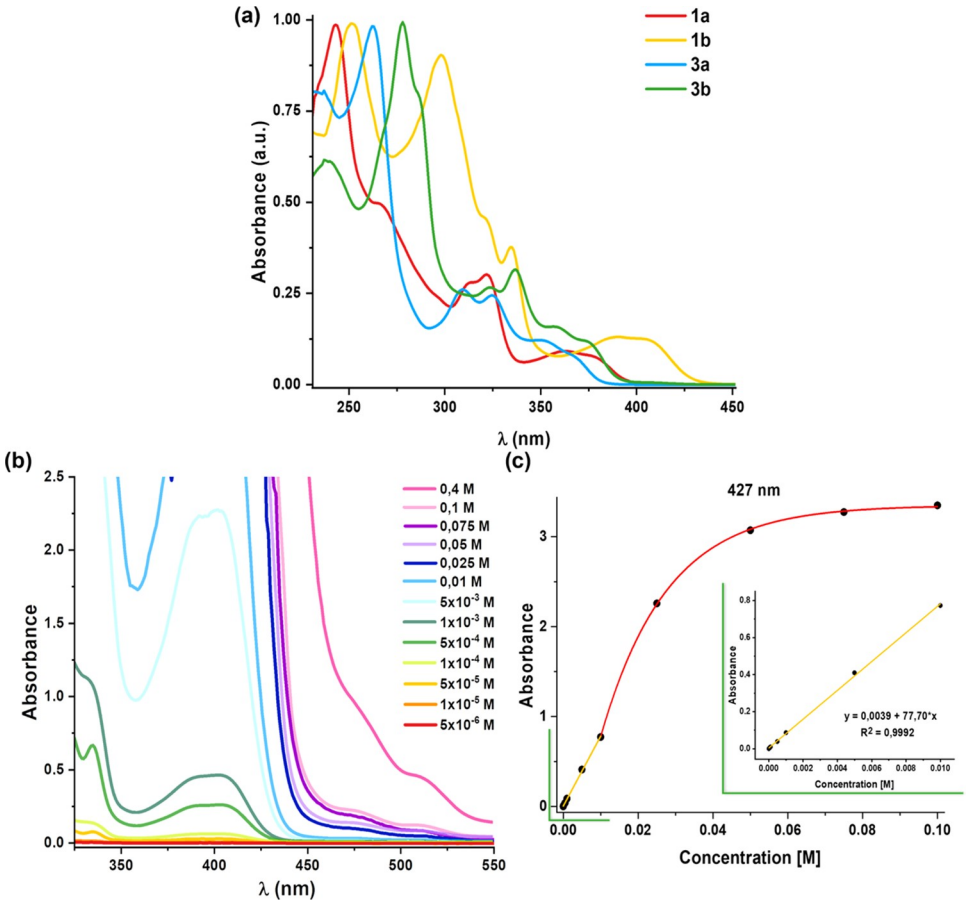

Figure 4. (a) Normalized absorption spectra of complexes **1a**, **1b**, **3a**, and **3b** in CH_2Cl_2 at 298 K. (b) Low-energy region of the UV−vis absorption spectra of **1b** in CH_2Cl_2 at different concentrations. (c) Representation of the absorbance at the 427 nm band *vs* concentration. Green box: the expansion of the low concentration range (<0.01 M).

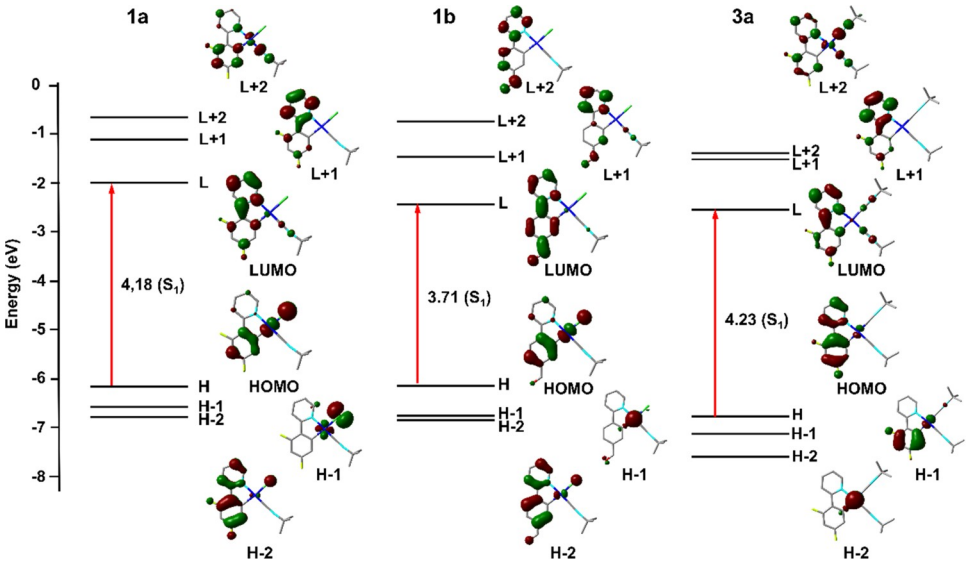

Figure 5. Schematic representation of selected frontier orbitals and excitations of **1a**, **1b**, and **3a**.

solution (5×10^{-5} M, Figure 4), and also in THF for compounds **1** (Figure S12), and the data are listed in Table S6. All complexes display intense high-energy absorption bands till ∼340 nm, assigned to a mixed intraligand ^{1}IL(π−π^*), located on the metalated C^N ligand and charge-transfer (^{1}MLCT/^{1}L′LCT/^{1}LL′CT) transitions. They also show a characteristic low-energy (LE) broad feature, red-shifted for the ppy-CHO compounds (**b**) in relation to that of dffpy (**a**) (389, 408 **1b** *vs* 362, 379 **1a**; 360, 375 **3b** *vs* 351, 368 nm **3a**) and for the neutral Cl/CNBu^t (**1**) in relation to the cationic $(CNBu^t)_2$ (**3**), as expected on the basis of the lower energy of the corresponding lowest unoccupied molecular orbital (LUMO)

https://doi.org/10.1021/acs.inorgchem.2c01400
Inorg. Chem. 2022, 61, 10898−10914

Table 2. Photophysical Data for 1−3 (a, b) in the Solid State at 298 and 77 K

	298 K			77 K	
compound	λ_{em}/nm (λ_{ex}/nm)	$\tau/\mu s$	ϕ	λ_{em}/nm (λ_{ex}/nm)	$\tau/\mu s$
1a	625 (420)	1.1 (63%), 0.5 (37%)	0.51	650 (420)	7.5
1a-CHCl$_3$-R	662 (550)	0.24 (80%), 1.05 (20%)	0.21	660, 720$_{max}$ (470)	9.5 (660)
				730 (580)	3.7 (717)
					4.2 (730)
1a-CHCl$_3$-G	474$_{sh}$, 534[a] (420)	0.26 (51%), 1.68 (49%) (474); 22.7 (534)	0.11	474[a] (440)	12.4
1a-CHCl$_3$-G-ground	632 (460)	0.31 (35%), 1.35 (65%)	0.38	677 (468)	5.5
1a(THF)	627 (470)	0.3 (31%), 1.0 (69%)	0.43	654 (470)	8.9
1a(MeOH)	650 (525)	0.3 (70%), 0.9 (30%)	0.14	722 (530)	3.9
1a(EtOH)	651 (550)	0.4 (50%), 1.3 (50%)	0.26	718, 748$_{sh}$ (500)	4.3 (718)
					2.5 (748)
1a(CHCl$_3$)	660 (570)	0.3 (67%), 0.7 (33%)	0.22	724 (570)	3.2
1a(CH$_2$Cl$_2$)	689 (570)	0.2 (54%), 0.9 (46%)	0.21	739 (570)	2.3
1b	545[a] (420)	0.3 (53%), 2.8 (48%)	0.06	550 (420)	22.6
1b·0.5Toluene	658	<1%	0.20	550$_{sh}$, 596, 706 (420)	14.8 (550)
				706 (550)	12.6 (596)
					9.8 (706)
1b-ground	550[a] (420)	0.32 (64%), 1.96 (36%)	0.03 (420)	557, 598, 660 (420)	17.2 (557)
	660 (500)	(585)	0.05(500)		10.2 (660)
2a	640 (550)	0.22	0.05	717 (550)	2.1
2b				650 (515)	2.0
3a	474,[a] 595$_{max}$ (385)	1.4 (595)	0.57	478[a], 585$_{max}$ (385)	40.7 (478)
				478[a], 617$_{max}$ (420)	8.9 (617)
3a·0.25CH$_2$Cl$_2$	490, 509$_{max}$ (420)	24.8 (509)	0.15	488 (420)	47.4 (488)
3a-CHCl$_3$	627 (430)	1.09	0.26	482[a], 624$_{max}$, 638$_{sh}$, 721$_{sh}$ (430)	32.5 (482)
					10.8 (624)
				650 (475)	9.3 (650)
				725 (590)	1.4 (700)
3a-Acetone	612 (430)	0.4	0.15	480[a], 514, 613$_{max}$, 645$_{sh}$, 704$_{sh}$ (430)	67.3 (476)
				640, 659, 696$_{sh}$ (475)	10.7 (613)
				630, 690$_{max}$ (550)	9.5 (650)
					1.5 (690)
3a-THF	623 (430)	0.6	0.16	476, 510, 616$_{max}$, 705$_{sh}$ (430)	54.6 (476)
					12.5 (616)
				645 (470)	6.8 (645)
				630, 700 (540)	2.4 (700)
3b	530 (440)	0.1 (58%), 0.8 (43%)	0.10	560, 628 (480)	15.8

[a] $\nu_{0\rightarrow0}$ transition of the structured emission.

and the highest occupied molecular orbital (HOMO), respectively (ppy-CHO *vs* dfpy on the LUMOs and cationic *vs* neutral on the HOMOs). The absorption spectra in CH_2Cl_2 and THF display similar patterns, with a slight negative solvatochromism for the LE band with a red shift on decreasing the polarity of the solvent (362, 379 **1a**, 389, 408 **1b** nm in CH_2Cl_2; 382 **1a**, 392, 412 nm **1b** THF), evidencing a certain charge-transfer (CT) nature (Figure S12).

DFT/time-dependent (TD)-DFT calculations were carried out for monomeric species of **1a**, **1b**, and **3a** in CH_2Cl_2 (Tables S7−S9 and Figures S13−S16). In complexes **1**, the low-energy feature is mainly assigned to a ^{1}IL/^{1}MLCT admixture with some ^{1}XLCT (X = Cl) character, whereas bis-isocyanide complex **3a** has an important ^{1}IL character, with some ligand-to-ligand (^{1}LL′CT, C^N → C≡N) and ligand-to-metal ^{1}LMCT character. The red shift observed for the ppy-CHO complexes (**b**) in relation to the dfppy (**a**) can be related to the stabilization of the LUMO induced by the presence of the aldehyde moiety (−1.98 **1a** *vs* −2.43 eV **1b**), whereas the HOMO remains similar (−6.16 **1a** *vs* −6.14 eV **1b**), which reduces the HOMO−LUMO gap. As is shown in Figure 5, the substitution of the chloride by other isocyanide ligand displays a blue shift in the LE absorption maxima (362, 379 **1a** *vs* 351, 368 nm **3a**), which can be ascribed to the major C^N contribution in **3a** (94%) with respect to **1a** (55%) in the HOMO and to the π-acidity of the isocyanide that stabilizes the HOMO, leading to a larger HOMO−LUMO gap.

A concentration dependence study in CH_2Cl_2 was carried out for **1a** and **1b**. In both complexes (Figure 4b,c for **1b**, and Figure S17 for **1a**), the lowest absorption band follows Beer's law in the concentration range from 5×10^{-6} to 5×10^{-3} M, suggesting that no obvious ground-state aggregation occurs within these concentrations range. However, at higher concentrations (>5×10^{-3} M), a clear deviation from Beer's law is observed for **1b** (monitored at 427 nm). Weaker absorptions are also discernible at lower energy (~475 and 510 nm), indicating the formation of aggregates. This agrees with color and emission changes from pale-yellow to dark orange on increasing the concentration from 5×10^{-3} to 0.4 M. This aggregation is also reflected in the clear upfield shift of all aromatic proton signals upon increasing the concentration (Figure S18). However, complex **1a** exhibited lower solubility at concentrations >5×10^{-3} M, and the study is less conclusive.

https://doi.org/10.1021/acs.inorgchem.2c01400
Inorg. Chem. 2022, 61, 10898−10914

Emission Spectra in the Film, Solution, and TD-DFT Calculations. Photophysical properties of complexes **1a**, **1b**, **3a**, and **3b** were studied in doped polystyrene (PS) films (1−10 wt %) and CH_2Cl_2 and THF solutions (298, 77 K) and in the solid state; the relevant data are listed in Tables S10 and 2. Calculations on the lowest-lying (S_0−T_1, SI) and spin density distribution of the triplet excited states (T_1) based on their corresponding optimized S_0 and T_1 geometries of the monomers are detailed in the SI.

Both chloride−isocyanide derivatives **1a** and **1b** display in a diluted PS film (1 wt %) structured phosphorescence bands (λ_{em} = 467 **1a**, 524 nm **1b**, Figures 6 and S19), attributed to monomer

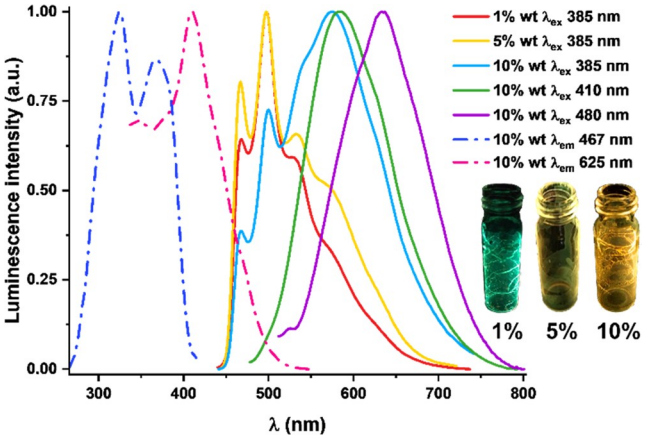

Figure 6. Normalized excitation (dashed line) and emission (solid line) spectra in PS at 1−10 wt % at 298 K in air of **1a**.

emission (^{3}IL/^{3}MLCT) involving the cyclometalated ligand and the Pt atom, with a predominant ^{3}IL character (see calculations below). At higher concentrations, only **1a** forms aggregates. Thus, at a doped concentration of 10 wt %, a broad unstructured red-shifted emission band appears at ∼580 nm, increasing in intensity relative to the peak at 467 nm by excitation from 365 to 410 nm and only a broad red-shifted band at 635 nm with λ_{exc} > 460 nm. These bands are characteristic of the formation of partial ground-state aggregates formed by $\pi\cdots\pi$ stacking and/or Pt···Pt interactions, which are supported by the different excitation spectra obtained by monitoring the distinct emission maxima. Because of these contributions, the emission color shifts gradually from green to yellow-orange with increasing concentration (Figure 6), and the quantum yields increase from ϕ = 5% (PS 1 wt %, monomer) to 19% (PS 10 wt %), although without a significant effect in the lifetimes, which fit to two components ($\tau_{average}$ = 0.6−0.9 μs).

Only **1b** is emissive in fluid CH_2Cl_2 (5×10^{-4} M) at 298 K (Figure S20), displaying a typical structured phosphorescent emission, indicative of an emissive state of mixed ^{3}IL/^{3}MLCT nature with a dominant ^{3}IL character, which was further supported by calculations (see below). No significant changes neither in emission maxima nor the quantum yield were observed in a THF solution at 298 K (Table S10). Complex **1b** shows an aggregation of the Pt^{II} monomer in glasses of CH_2Cl_2 even in a diluted solution (5×10^{-5} M, λ_{em} 640 nm), whereas in THF glasses, the presence of the monomer (λ_{em} 517 nm, Figure S20) is dominant. The effect of the concentration on the emissive behavior was examined in CH_2Cl_2 at 298 and 77 K. The distinct emission profiles and color change can be visualized in Figure S21. At 298 K, increasing the concentration (5×10^{-5} to 0.4 M) affects the emission color. With concentrations of 5×10^{-5} to 0.01 M, only the monomer is observed. From 0.01 to 0.4 M, an aggregation broad peak (λ_{em} ∼ 710 nm), attributed to metal−metal-to-ligand charge transfer (^{3}MMLCT), gradually gains intensity, and the emission changes from green to red (Figure S21a). Upon cooling to 77 K, the monomer emission dominates in diluted solutions (5×10^{-5} to 10^{-3} M), whereas that aggregated emission peak is observable from 0.01 to 0.4 M, together with the monomer (Figure S21b).

Complex **1a** is nonemissive in solution probably due to deactivation through molecular motions in fluid or the ease of the thermal activation of the ^{3}MC excited states. In a glassy solution at 77 K, it exhibits intense emission profiles, which depend on the solvent, the concentration, and the wavelength excitation. Upon cooling, diluted CH_2Cl_2 solutions (5×10^{-5} M) show three different emission bands depending on the excitation wavelengths (Figure 7). By excitation to low

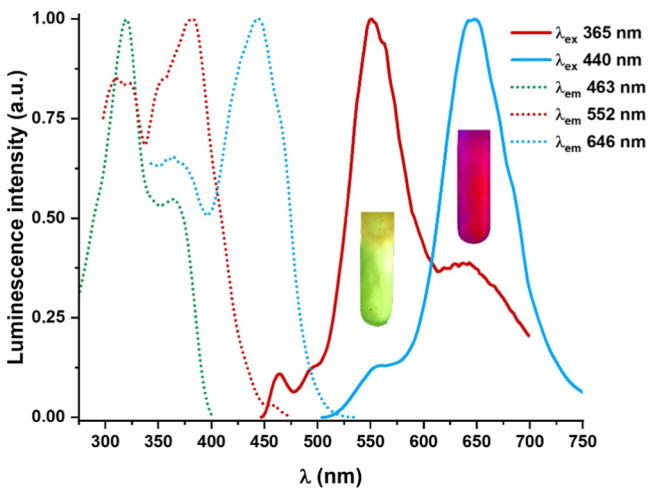

Figure 7. Normalized excitation and emission spectra of **1a** in CH_2Cl_2 5×10^{-5} M at 77 K. Photographs taken under lamps of the ∼λ_{exc} indicated and the N_2 atmosphere.

wavelengths (λ_{exc} 365 nm), a minority band of the monomer (λ_{em} 465 nm), a broad band at 552 nm, and a shoulder at 645 nm are observed, whereas with λ_{exc} > 440 nm, the band at 645 nm dominates. The excitation spectra monitored at the three peaks differ, also suggesting the aggregation processes. At higher concentrations (5×10^{-4} M), only two broad emission bands (λ_{em} 570 and 650 nm) are observed by excitation at λ_{exc} < 400 nm, the LE emission band being selectively obtained using LE excitation wavelengths (λ_{exc} 450 nm) (Figure S22). Considering the unstructured emission profiles and their crystal packing, we tentatively ascribe the origin of these LE bands to ligand-centered $^3\pi\pi^*$ and ^{3}MMLCT transitions, respectively. Similar behavior was observed in THF at 77 K (Figure S23). In the glasses, the aggregate lifetimes [τ = 9.7 μs (552), 6.4 μs (645 nm) **1a**, CH_2Cl_2 5×10^{-5} M; 10.1 μs (640 nm) (5×10^{-5} M), 9.7 μs CH_2Cl_2 0.01 M, **1b**] are shorter than the corresponding monomer decay [τ = 14.9 μs (465), **1a**, CH_2Cl_2; 14.8 μs (540) CH_2Cl_2 **1b**], in agreement with ^{3}MMLCT contribution for the lowest-energy band (645 **1a**, 710 nm **1b**) or some triplet−triplet annihilation (TTA)[25] in the $^3\pi\pi^*$ excimeric-like feature (552 **1a**, 640 nm **1b**).

For the bis-isocyanide compounds in PS films (1 wt %), **3b** displays a typical ^{3}IL-structured emission (524 nm), similar to **1b**, while in the dfppy derivative (**3a**) dominates an unstructured

https://doi.org/10.1021/acs.inorgchem.2c01400
Inorg. Chem. 2022, 61, 10898−10914

emission peak [600 nm, τ = 1.8 (61%), 3.0 (39%) μs], characteristic of aggregate emission, in relation to the small intensity of the monomer (474 nm) (Figure 8). In a fluid

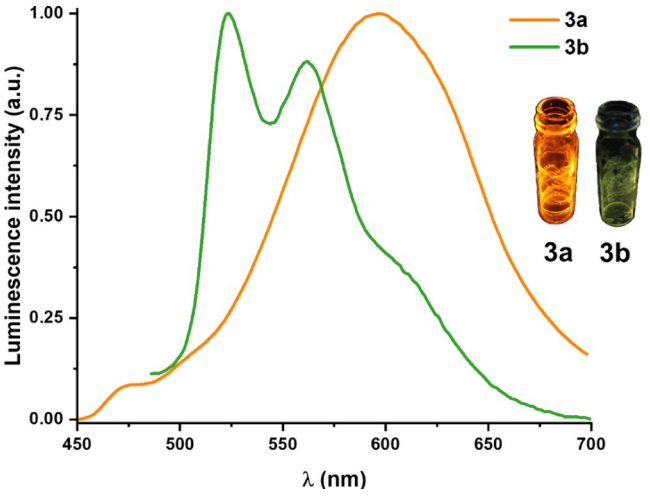

Figure 8. Normalized emission spectra of **3a** (λ_{ex} 365 nm) and **3b** (λ_{ex} 420 nm) in PS (1 wt %) at 298 K in air.

CH_2Cl_2 solution (5×10^{-4} M) (Figures S24a and S25a) both compounds show monomer emission (471 **3a**, 511 nm **3b**) with lower quantum yields (ϕ 1% **3a**, 2% **3b**) than in PS films (ϕ 27% **3a**, 9% **3b**). In agreement with its behavior in PS films, compound **3a** shows a higher tendency to aggregate in glasses at 77 K (Figure S24b), whereas **3b** displays essentially monomeric emission with an increase in the LE shoulder (Figure S25b). As in complexes **1**, the aggregate lifetimes [τ = 6.6 (580) **3a**, 14.5 (618) μs **3b**, CH_2Cl_2 77 K] are shorter than the corresponding monomer [τ = 39.1 (475) **3a**, 24.5 (524) μs **3b**, CH_2Cl_2 77 K].

The analysis of the monomer emission of these compounds indicates that the variation of the cyclometalated ligand has a notable effect on the emission maximum, with the ppy-CHO complexes (**b**) red-shifted with respect to the dfppy (**a**) derivatives, consistent with the higher energy gap for the $\pi-\pi^*$ orbitals of the dfppy complexes. The nature of the emissions was studied in **1a**, **1b**, and **3a** through calculations of the lowest-lying T_1 ($S_0 \rightarrow T_1$) (Table S9) and spin density distribution for the triplet excited states (T_1) (Figure 9), based on their corresponding optimized S_0 and T_1 geometries, respectively. The calculated lowest-lying T_1 state involves mainly the HOMO → LUMO transition (66% **1a**, 77% **1b**, 83% **3a**), resulting in a ^{3}IL transition with a minor contribution of ^{3}MLCT and ^{3}XLCT for complexes **1** and ^{3}LL′CT (C^N → CNBu^t) and ^{3}LMCT (C^N → Pt) for **3a**. However, the calculated spin density distribution in the optimized T_1 state (Figure 9) is located mainly on the cyclometalated ligand and to a lesser extent in platinum (Pt, 0.1377 **1a**, 0.1912 **1b**, 0.0850 **3a**), with a negligible contribution of the other coligands, thus supporting a predominant ^{3}IL state with ^{3}MLCT contribution higher in the neutral complexes **1** than in **3**. This result is in coherence with numerous works on cyclometalated isocyanide metal complexes, in which the large separation between the ^{3}MLCT and ^{3}IL states lead to a weak configuration interaction and a predominant ^{3}IL character in T_1.[26] In agreement with this, the calculated contribution of the Pt center in the SOMO-1 (Figure S26 and Table S11) decreases (Pt 9% **1a**, 16% **1b**, 3% **3a**) in the optimized T_1 state in relation to the optimized S_0 geometry, especially for **1** (HOMO, 30% **1a**, 34% **1b**, 5% **3a**), suggesting distortion upon excitation. The calculated emission wavelengths [**1a** (521), **1b** (619), **3a** (531 nm)] are consistent with the monomer emission observed [**1a** (467), **1b** (524), **3a** (474 nm), PS 1 wt %], although with expected overestimated values.

Emission Spectra in the Solid State. The photophysical characteristics in the solid state are compiled in Tables 2 (emission) and S12 (absorption spectra calculated from their reflectance spectra). Interestingly, complexes **1a** and **1b** exhibit multistimuli behavior, and **3a** shows vapochromic behavior. As is seen in the structural section, the different possibility of packing of the complexes seems to be decisive in the observed vapochromic (**1a**, **1b**, **3a**), solvatochormic, and mechanochromic (**1a**, **1b**) behavior.

Powdered as-obtained yellow-orange samples or crystals of **1a** show a bright orange structureless emission band (625 nm), narrower and red-shifted (650 nm) to 77 K (Figures 10 and S27), which is associated with a mixed ^{3}MMLCT/$^3\pi\pi^*$ manifold due to the formation of dimers in the ground-state stacking in columns with relatively close Pt···Pt and $\pi\cdots\pi$ contacts. However, crystals of **1a·CHCl$_3$** display a yellow-green monomer ^{3}IL/^{3}MLCT emission (534 nm) with a minor structured ^{3}IL band at 474 nm, which dominates at 77 K (Figure S28), in accordance with their staggered columnar packing with longer Pt···Pt separations. Interestingly, upon fuming the yellow-orange powder **1a** with vapors of $CHCl_3$ for only ∼5 min, the sample changes to a kinetic red form, with a red emission (**1a-CHCl$_3$-R** form) (Figures 10a and S29). The elemental and thermogravimetric analyses (TGA) of the **1a-CHCl$_3$-R** form revealed a phase transition at 75 °C arising from the desorption of $CHCl_3$ from the lattice (Figure S30a). When a red sample of **1a-CHCl$_3$-R** was heated up to 175 °C, the lost weight (*ca.* ∼19%) corresponds to about one lattice $CHCl_3$

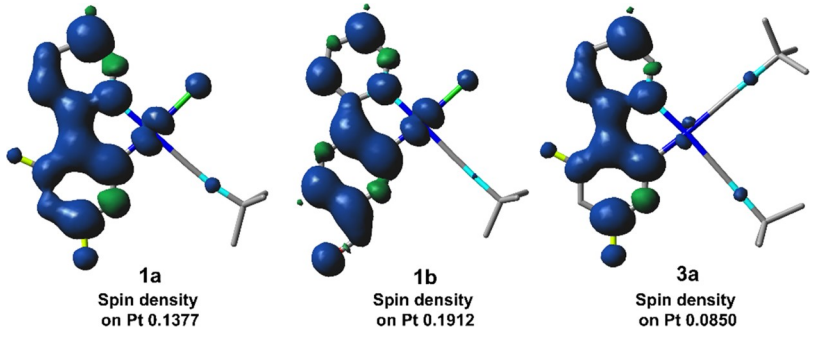

Figure 9. Spin density distribution for the lowest triplet excited state in **1a**, **1b**, and **3a**.

https://doi.org/10.1021/acs.inorgchem.2c01400
Inorg. Chem. 2022, 61, 10898−10914

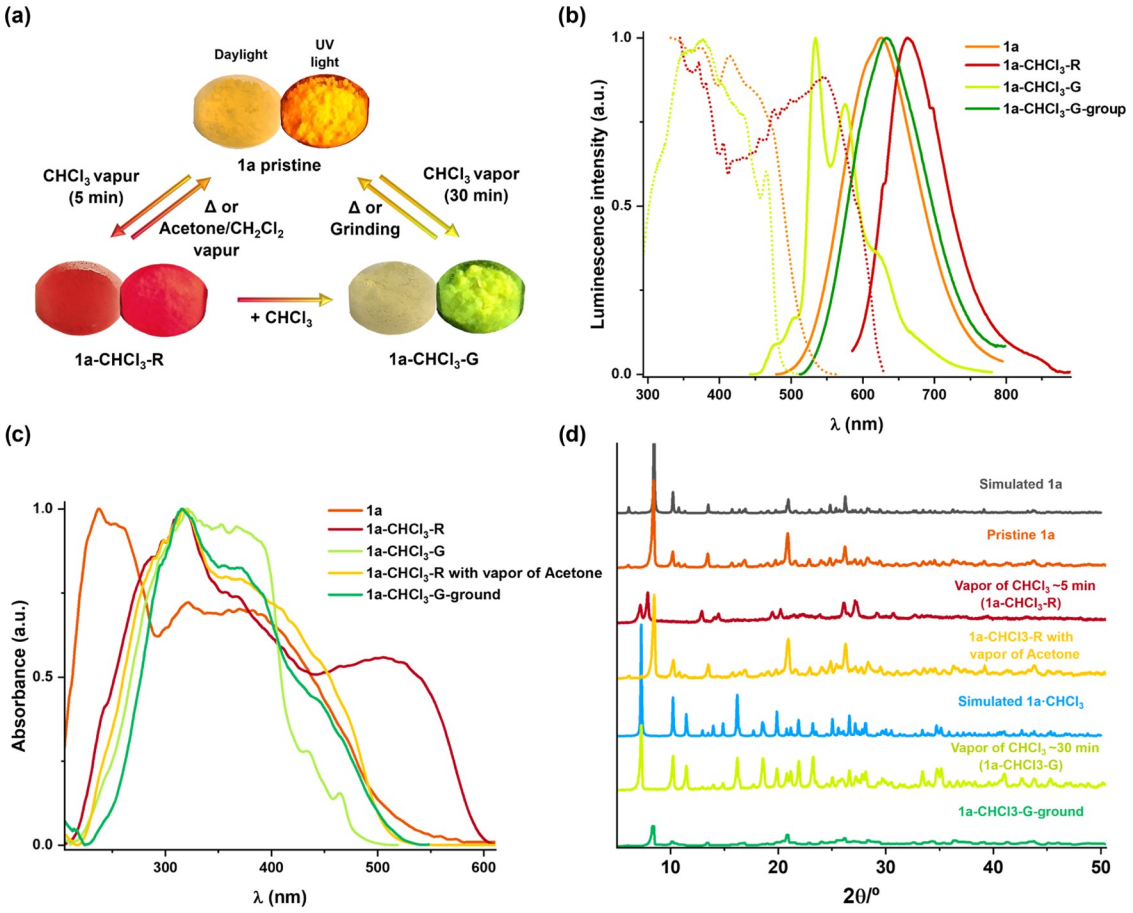

Figure 10. (a) Scheme and photographs of the external stimuli-responsive color and emission changes in **1a**; left: under ambient light and right: under UV light irradiation (λ_{ex} 365 nm). Emission color changes of **1a** after exposure to $CHCl_3$ vapors for 5 min (**1a·CHCl$_3$-R**) or more than 30 min (**1a·CHCl$_3$-G**). (b) Normalized excitation (red, λ_{em} 660 nm; orange λ_{em} 625 nm; green λ_{em} 535 nm) and emission spectra of **1a** powder (λ_{ex} 420 nm), **1a·CHCl$_3$-R** (λ_{ex} 550 nm), **1a·CHCl$_3$-G** (λ_{ex} 400 nm), and **1a·CHCl$_3$-G-ground** (λ_{ex} 450 nm) in air. (c) Normalized absorption spectra calculated from their reflectance spectra in the solid state. (d) Powder XRD (PXRD) patterns of different forms of **1a**.

molecule per complex, giving **1a**. This **1a-CHCl$_3$-R** form displays a red shift structureless band centered at 662 nm, which narrows and considerably shifts to lower energies (λ_{max} 730 nm, λ_{exc} 580 nm) at 77 K (Figure S29). The emission is attributed to an ^{3}MMLCT transition from long-range kinetic aggregates (trimers, tetramers, etc.) formed by fast incorporation of the solvent and likely having shorter Pt···Pt intermolecular interactions than that found in **1a**. Interestingly, $CHCl_3$ is easily removed in this kinetic red form (**1a-CHCl$_3$-R**), and upon treatment with acetone or CH_2Cl_2 vapors, the unsolvated **1a** is recovered. By contrast, if the fuming time of **1a** with vapors of $CHCl_3$ increases to ∼30 min at 298 K, we observed that the color changes gradually from red (**1a-CHCl$_3$-R**) to a final thermodynamically more stable yellow form (**1a-CHCl$_3$-G**) (Figure 10a), with a green-yellow structured emission identical to that measured for crystals **1a·CHCl$_3$**. TGA analysis shows a phase transition from **1a-CHCl$_3$-G** at 75 °C, corresponding to the transformation to **1a**, by the loss of $CHCl_3$ (Figure S30b). If the solid **1a-CHCl$_3$-G** is kept in a close vial, it is stable for weeks, but if it is heated to 65 °C, it reverts to **1a**, although without passing through the previous kinetic red form. Interestingly, the color of the phase **1a-CHCl$_3$-G** changed from pale-yellow to dark yellow by manual grinding in a mortar (Figure S31). The **1a-CHCl$_3$-G-ground** form is an amorphous orange emissive phase, which displays a broad unstructured band at 632 nm, similar to the as-prepared powder **1a**, which is red-shifted at 77 K (677 nm). This indicates that mechanical stress in the yellow phase favors the ground-state interchromophore interactions. The emission quantum yields of these forms range from ϕ 11% in **1a-CHCl$_3$-G**, 21% **1a-CHCl$_3$-R**, and 38% **1a-CHCl$_3$-G-ground** to 51% **1a** (Table 2). These values are comparable to or higher than those in polystyrene.

The absorption properties of all forms in the solid state are shown in Figure 10c and Table S12. The yellow-orange pristine solid **1a** shows a broad absorption band up to 550 nm, whereas the **1a-CHCl$_3$-G** form is characterized by a blue-shifted absorption band up to 500 nm, attributed to mixed ^{1}LLCT/^{1}MLCT transitions. The **1a-CHCl$_3$-R** phase shows an absorption spectrum extending to 600 nm, most likely due to ^{1}MMLCT transitions based on Pt···Pt interactions, in coherence with its color. As expected, the absorption spectrum of **1a-CHCl$_3$-G-ground** and **1a-CHCl$_3$-R** treated with acetone vapors are similar to that obtained for pristine **1a**. The powder X-ray diffraction (PXRD) patterns show that pristine **1a** is crystalline in nature, the PXRD peaks being consistent with the major diffraction peaks simulated from the cif files of the structure of larger single crystals of **1a** (Figure 10d), suggesting that microcrystalline solid has a molecular packing similar to that of their larger crystalline samples. After exposing the sample of **1a** to $CHCl_3$ fumes for 5 min to obtain the red form **1a-CHCl$_3$-R**, new peaks appeared (red line), indicating that the

https://doi.org/10.1021/acs.inorgchem.2c01400
Inorg. Chem. 2022, 61, 10898−10914

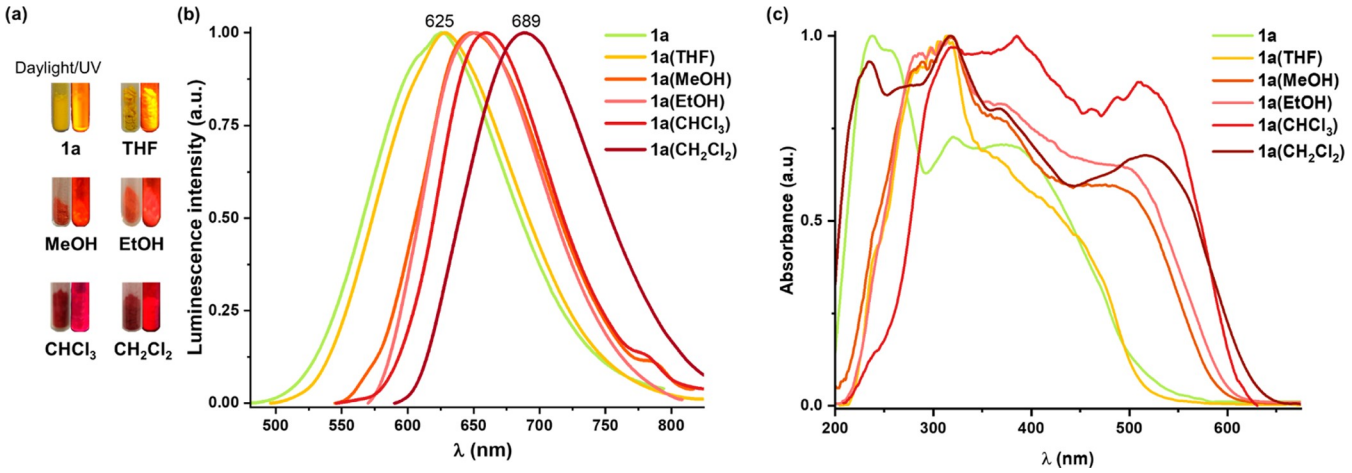

Figure 11. (a) Photographs under ambient light, air atmosphere, and UV light irradiation (λ_{ex} = 365 nm) of **1a** (solid) and solids obtained by the evaporation of the appropriate solution of **1a** in different solvents. (b) Normalized emission spectra. (c) Normalized absorption spectra calculated from their reflectance spectra in the solid state.

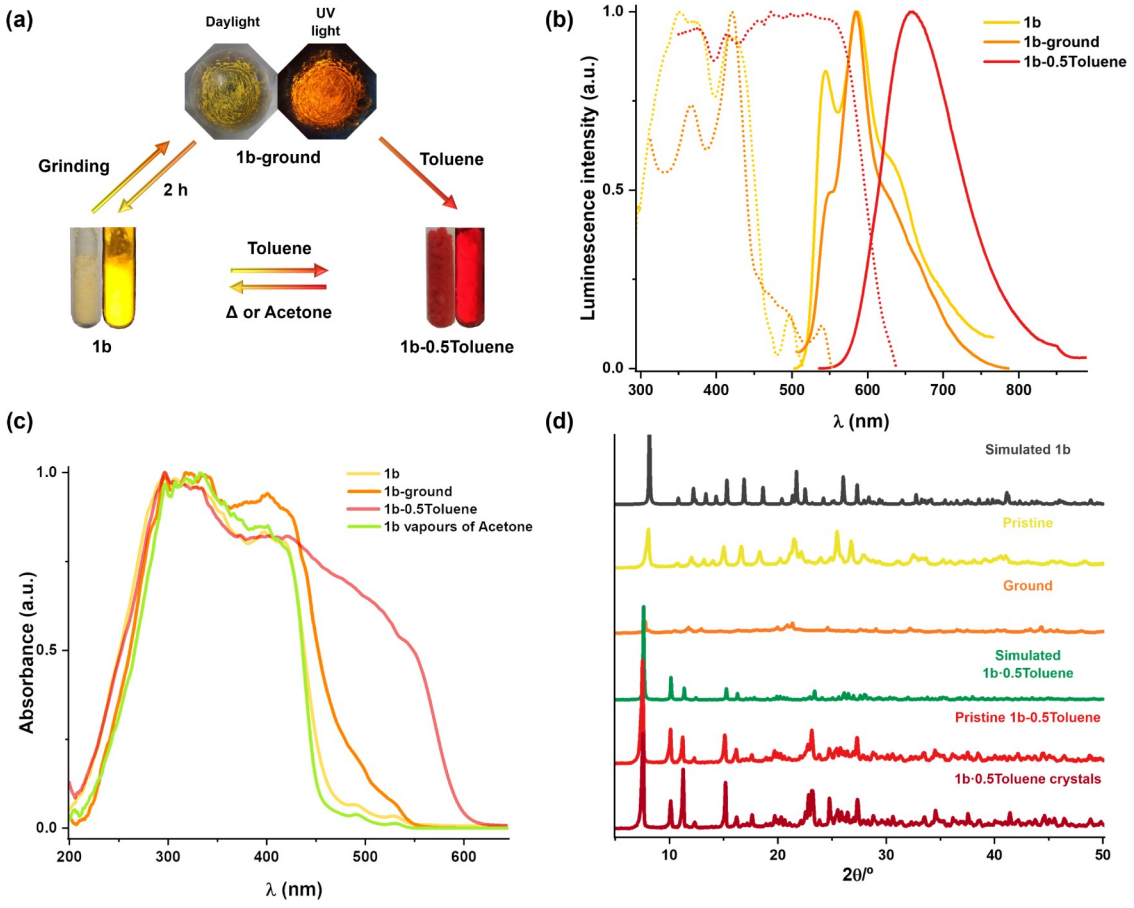

Figure 12. (a) Scheme and photographs of the external stimuli-responsive color and emission changes in **1b**; left: under ambient light and right: under UV light irradiation (λ_{ex} 365 nm). The emission color of **1b** changes under treatment with toluene vapors for 2 h or addition of a drop of toluene (**1b·0.5Toluene**) and by mechanical grinding to afford **1b-ground**. (b) Normalized excitation (yellow, λ_{em} 544 nm; orange, λ_{em} 585 nm; red, λ_{em} 660 nm) and emission spectra of **1b** (λ_{ex} 430 nm), **1b·0.5Toluene** (λ_{ex} 480 nm), and **1b-ground** (λ_{ex} 420 nm) in air. (c) Normalized absorption spectra calculated from their reflectance spectra in the solid state. (d) Powder XRD patterns of different forms of **1b**.

incorporation of a molecule of $CHCl_3$ induces a structural transformation. The peaks of the pristine sample **1a** can be mainly recovered once the red sample **1a-CHCl$_3$-R** is exposed to acetone or CH_2Cl_2 vapors or is heated above 75 °C (yellow line, Figure 10d), indicating that both phases are dynamically related and that the positions of $CHCl_3$ are not occupied by the incoming solvents. This behavior suggests the ease of loss of $CHCl_3$ either by displacement with more volatile vapors or by heating above the boiling point of $CHCl_3$ (61 °C). The vapochromic luminescent behavior of **1a** in $CHCl_3$ and **1a-**

https://doi.org/10.1021/acs.inorgchem.2c01400
Inorg. Chem. 2022, 61, 10898−10914

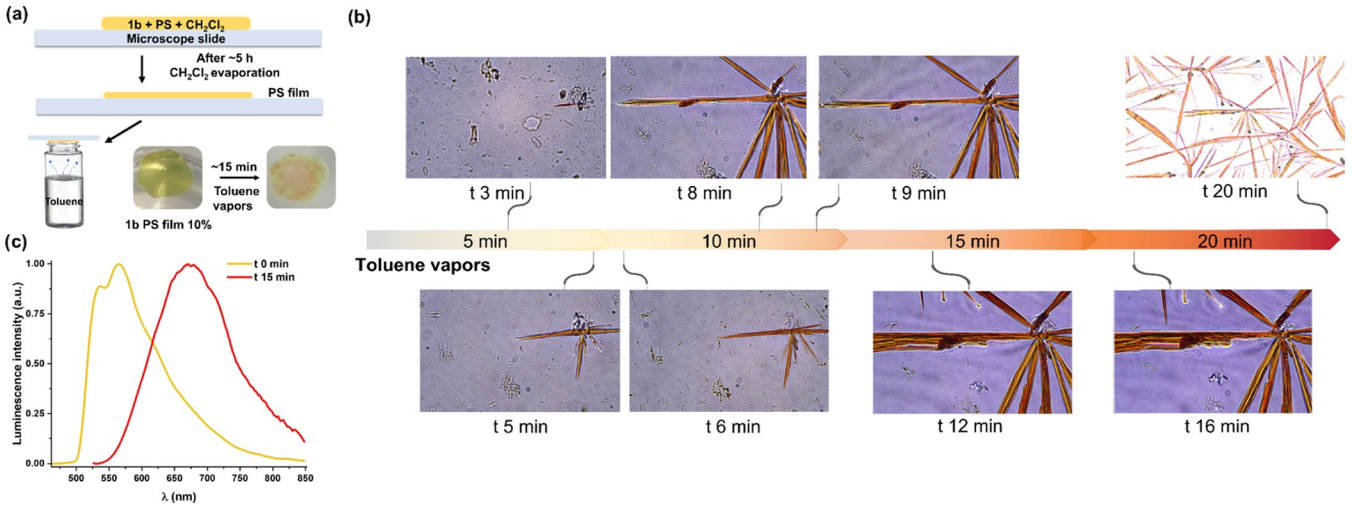

Figure 13. (a) Schematic drawings showing the fabrication of the PS film and the exposition to toluene vapors. Naked eye images of the PS film of **1b** doped at 10% under room light before and after the toluene vapors. (b) Microscopy images of the PS film while the crystals grow by exposure to the solvent for more than 20 min. Images up to 16 min have a magnification of 40× (numerical aperture 0.95), while the image of 20 min has a magnification of 10× (numerical aperture 0.45). (c) Emission color changes of **1b** in a film of PS at 10% (line yellow, λ_{ex} 400 nm) and after exposition to toluene vapors (line red, λ_{ex} 500 nm) at 298 K.

$CHCl_3$-R in acetone is reversible for at least five cycles without perceivable performance degradation (Figure S32). Furthermore, when the red sample **1a-$CHCl_3$-R** is exposed to air without stimuli, it gradually changes its color and emissive behavior from red to yellow-orange (more than 2 weeks), indicating that the desolvated **1a** species is recovered. On the other hand, the PXRD peaks of the pale-yellow solid **1a-$CHCl_3$-G**, obtained by treatment of **1a** with vapors of $CHCl_3$ for ∼30 min (green line, Figure 10d), show consistency with the major diffraction peaks simulated from the cif file of crystals of **1a·$CHCl_3$** (blue line). Finally, the grinding process of **1a-$CHCl_3$-G** induces a considerable decrease in its crystallinity, transforming it into an amorphous phase.

In addition to responding to vapors and pressure, complex **1a** displays reversible color, color emission, and quantum efficiency change depending on the crystallization solvents (Figure 11a). The colors of the solids obtained by evaporation after the dissolution of **1a** in different solvents vary from yellow to red and the emission ranges from 627 nm (THF) to 689 nm (CH_2Cl_2) (Figure 11b), red-shifted at 77 K (654 nm, THF to 739 nm, CH_2Cl_2) (Figure S33 and Table 2). With MeOH or EtOH, the shift observed is ∼25 nm (298 K)/∼70 nm (77 K) and with $CHCl_3$ or CH_2Cl_2 it reaches up to ∼64 nm (298 K)/∼90 nm (77 K). This discernible behavior can be also observed in the UV−vis absorption solid spectra. The solids obtained from alcohols show, in relation to **1a**, a red-shifted LE band up to 550 nm and from chloride solvents up to 630 nm (Figure 11c and Table S12). The notable red shift of the red solvates could be mainly ascribed to ^{1}MMLCT transitions favored by the presence of different aggregates with distinct $\pi\cdots\pi$/Pt···Pt interactions, which seems to be stronger in chloride solvents. The emission color changes are accompanied by a dramatic decrease in the emission brightness from ϕ = 51%, **1a** to 14%, **1a(MeOH)**, typically attributed to aggregation caused quenching. Interestingly, the formed phases in these solvents are not stable with time and the initial form **1a** (emission and quantum efficiencies) can be restored on standing *ca.* 72 h or by stirring the solids in hexane for 1 h. This fact suggests that crystallization from chloride solvents probably gives rise to structures with short Pt··· Pt distances, which slowly undergo switching to more stable structures surely with longer Pt···Pt separations.

Complex **1b** also exhibits remarkable luminescence switching properties as a result of their self-assembly behavior under application of different external stimuli. The two pseudopolymorphs, **1b** and **1b·0.5Toluene**, can be exchanged under vapor/solvent exposure or heating. Furthermore, a new phase (**1b-ground**), obtained by mechanical grinding of the monomer-emissive form **1b**, is described. The related luminescence images and emission spectra of the three phases are shown in Figure 12a,b. The yellow powder **1b** (and also microcrystals of **1b**) exhibits a yellow structured emission at 545 nm (ϕ = 6%), only slight red-shifted at 77 K (550 nm) and, as expected, with more prolonged lifetime (τ_{av} = 1.5 μs, 298 K; 22.6 μs, 77 K) (Figures 12 and S34). Red microcrystals of **1b·0.5Toluene** show a broad red emission at 658 nm with a ϕ value of 20% and a short lifetime (<1 μs) at 298 K, which is red-shifted at 77 K (706 nm; 9.8 μs) (Table 2 and Figure S35). This emission is ascribed to ^{3}MMLCT in accordance with the short Pt··Pt distance (3.362 Å) found in the crystals of **1b·0.5Toluene**. After **1b** was ground, the resulting amorphous orange-yellow powder (**1b-ground**) developed a lesser structured band at 550 nm upon excitation at 420 nm, and a broad LE band at 660 nm by exciting to 500 nm (Figure S36), which are red-shifted at 77 K, indicating the formation of an amorphous solid with closer Pt units. This solid is not stable and **1b** is recovered on standing by 2 h.

When samples of **1b** or **1b-ground** were exposed to toluene liquid or vapors (around 2 h), the yellow powder turned vivid red with red luminescence. The emission spectra displayed an identical pattern to those of the crystals of **1b·0.5Toluene**. The diffuse reflectance spectrum showed a broad band reaching 610 nm, clearly red-shifted in relation to those obtained with samples of **1b** or **1b-ground** tail to 550 nm) (Figure 12c). TGA of **1b·0.5Toluene** revealed the phase transition arising from desorption of the lattice toluene molecules because the TGA curve of up to ∼170 °C represented a weight loss of *ca.* 7.8% corresponding to a half molecule per complex, as the crystal structure of **1b·0.5Toluene** (Figure S37). However, on standing in the solid, the toluene molecules are also lost over time, and

https://doi.org/10.1021/acs.inorgchem.2c01400
Inorg. Chem. 2022, 61, 10898−10914

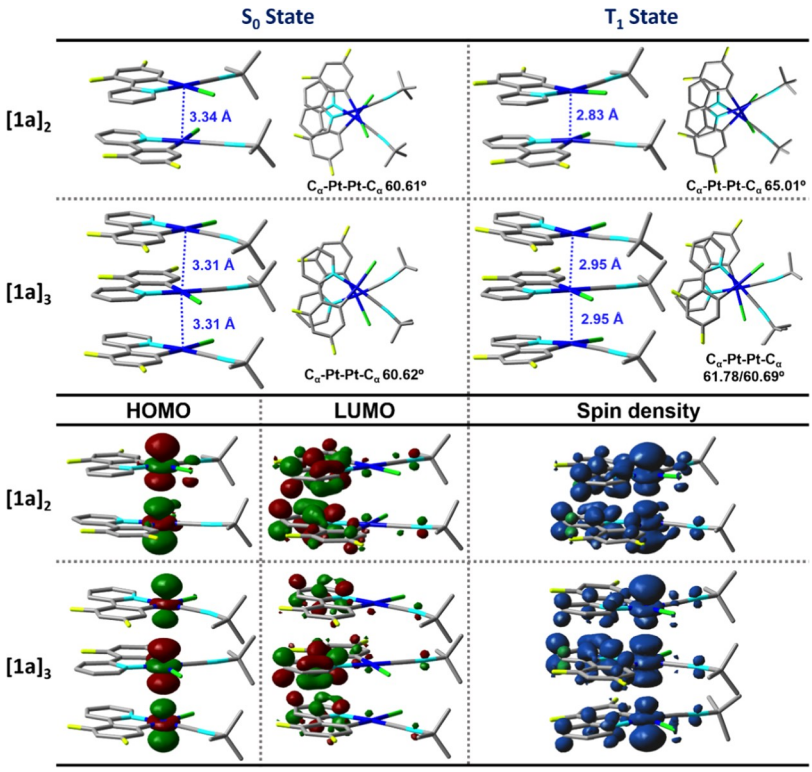

Figure 14. Optimized geometries of $[\mathbf{1a}]_2$ **and** $[\mathbf{1a}]_3$ models at the S_0 and T_1 states. Contour plots of HOMO and LUMO at the S_0 and spin density at the T_1-optimized geometries [B3LYP/6−31G(d,p)].

after 1 month of exposure to the air, it showed a gradual change to **1b** (Figure S38). Moreover, **1b** is recovered by exposition to acetone liquid/vapors or heating over 110 °C, as is reflected in its color change and its diffuse reflectance spectrum (Figure 12c).

The powder X-ray diffraction pattern of **1b** coincides well with the simulated powder pattern of $\mathbf{1b}_{crystal}$ (Figure 12d). Mechanical force destroys or changes the ordered molecular packing and induces a crystal-to-amorphous transformation in the PXRD pattern of **1b-ground**, forming a much looser packing where more active molecular motions can occur. A direct crystal-to-crystal phase transition from **1b** to **1b·0.5Toluene** was observed for the PXRD of **1b·0.5Toluene**, obtained from **1b** under saturated toluene vapor or $\mathbf{1b{\cdot}0.5Toluene}_{crystal}$, as shown in Figure 12d, which coincides with the simulated PXRD pattern of $\mathbf{1b{\cdot}0.5Toluene}_{crystal}$. Toluene fuming can facilitate molecular motions and lead to an arrangement of molecules to form ordered packing again.

Aggregation of Pt^{II} compounds embedded in polymeric matrices can lead to sensory properties, which are not present in the starting compound. This type of process has been studied in depth for its use as dyes in the fabrication of smart materials.[16a,27] In this sense, we decided to evaluate the self-assembly behavior of **1b** inside the polymer matrix. Two films of polystyrene (PS) were obtained after doping them with 1 and 10%, respectively, of **1b** in CH_2Cl_2. As is shown in Figure 13a, one drop of each mixture was deposited in a glass holder followed by slow evaporation at 298 K (∼5 h). To investigate if the compound **1b** inside the polymer exhibits vapochromic response, the two polymer thin PS films were exposed to vapors of toluene for 20 min, and then their luminescence was measured. For that, the glass with the thin film was placed on top of a vial containing toluene, allowing the vapor to come into contact with the polymer. In the case of the film doped at 1%, it exhibits the typical yellow emission of the monomer species (λ 524 nm). It seems that the low doping is not enough to self-assemble and form aggregates. However, for the higher concentrated film (10%), the change is notable in the presence of toluene vapor both in the naked eye and in the microscope (Figure 13b,c). In the beginning, the polymer film is a yellow-emitting (λ_{max} 566 nm) translucent sheet with some imperfect points. Within 3 min of being exposed to the solvent, orange-red crystalline needles grow inside the matrix from a starting nucleation point. After 15 min, multiple needles with a width of ∼50 μm have grown alongwith the film, showing a remarkable red shift of the emission with the aggregation band centered at 675 nm. This indicates that molecules are self-assembled *via* intermolecular $\pi\cdots\pi$ and/or Pt···Pt interactions. The emission of these orange-red needles resembles that of the **1b·0.5Toluene** crystals and the pristine solid **1b·0.5Toluene**, suggesting that the needles are formed by incorporation of toluene channels, as in the crystal packing. The needles are stable for more than 2 months inside the polymer matrix, but after that time, presumably, the toluene gradually is lost (Figure S39), losing its crystallinity and changing its color and emission to yellow.

The double salt **2a** is emissive in the solid state at 298 and 77 K and **2b** only at low temperature. **2a** shows a broad band centered at 640 nm (τ = 0.22 μs, ϕ = 5%), red-shifted to 77 K (717 nm, Δ = 77 nm; τ = 2.1 μs) and in relation to **2b** at 77 K (649 nm) that can be ascribed to a ^{3}MMLCT in the salt (Figure S40). Crystals of the cationic bis-isocyanide complex $\mathbf{3a{\cdot}0.25CH_2Cl_2}$ displays a monomer green phosphorescence (λ_{em} = 490 nm, ϕ = 15%, τ = 24.8 μs) at 298 K, more structured at 77 K (Table 2 and Figure S41a). However, **3a-pristine** solid shows a bright orange phosphorescence, with very high efficiency (ϕ = 57%) at 298 K, formed by a minor structured band corresponding to the

https://doi.org/10.1021/acs.inorgchem.2c01400
Inorg. Chem. 2022, 61, 10898−10914

monomer, together with a structureless band at 595 nm, red-shifted at 77 K (617 nm), ascribed to an ^{3}MMLCT emission. **3b-pristine** exhibits a broad feature, blue-shifted (λ_{em} = 530 nm) in relation to that observed in **3a-pristine** and with a lower quantum yield (ϕ = 10%), which might be attributed to excimer-like $^3\pi\pi^*$ emission (Figure S41b). At 77 K, it exhibits a dual emission with maxima at 560 and 628 nm, which is tentatively assigned to excimer-like $^3\pi\pi^*$ and ^{3}MMLCT, respectively. The solid **3a-pristine** showed reversible changes in its color and emission response to vapors of THF, acetone, and $CHCl_3$ at room temperature for 6 h. In all cases, there is a change in its color from pale-yellow to pinkish-orange, reflected in the diffuse reflectance spectra, which show new bands extending to ∼600 nm in relation to the **3a-pristine** (480 nm). In addition, the emission band is slightly red-shifted from 595 (**3a-pristine**) to 612 (**3a-acetone**), 623 (**3a-THF**), and 627 nm (**3a-CHCl$_3$**) (Figure S42). At 77 K, the solvate species exhibit a different pattern depending on the excitation wavelength (from 615 to 725 nm), suggesting the formation of different aggregates at low temperatures (Figure S43).

With the aim of understanding the observed red shift in the UV−vis absorption and emission spectra of the aggregated species, the geometries in the ground (S_0) and the first triplet excited (T_1) states of the dimer, trimer, and tetramer models were optimized in the gas phase based on **1a** and **1b** crystal structures. Two main intermolecular forces drive the dimer and tetramer assembly, the $\pi\cdots\pi$ and Pt···Pt intermolecular interactions. The geometries of calculated structures of $[\mathbf{1a}]_2$, $[\mathbf{1a}]_3$, and $[\mathbf{1b}]_4$ with their Pt···Pt distances and C_α−Pt−Pt−C_α angles and the orbitals involved in the electronic transitions (HOMO/LUMO) as well as the spin density plots are plotted in Figures 14 and S44. For **1a**, the computed Pt···Pt distance of the lowest-energy dimer $[\mathbf{1a}]_2$ and trimer $[\mathbf{1a}]_3$ in the S_0 is 3.34 and 3.31 Å, respectively, which is in agreement with the data of X-ray structural analyses. The metallophilic interactions are more evident in the T_1-optimized geometries ($[\mathbf{1a}]_2$ 2.83, $[\mathbf{1a}]_3$ 2.95 Å), being shorter than in the X-ray structure. The S_1 transitions of simulated $[\mathbf{1a}]_2$ and $[\mathbf{1a}]_3$ were mainly derived of the HOMO → LUMO transitions (>97%, Table S13). The HOMO is located at the Pt atoms (84% $[\mathbf{1a}]_2$, 86% $[\mathbf{1a}]_3$), whereas the LUMO is mainly localized in the dffpy cyclometalated ligand (84% $[\mathbf{1a}]_2$, 82% $[\mathbf{1a}]_3$), highlighting the prominent ^{1}MMLCT of the low-energy band, red-shifted in relation to the monomer (S_1 417 $[\mathbf{1a}]_2$, 488 $[\mathbf{1a}]_3$ *vs* 383 nm **1a**, Table 3). However, in the tetramer model $[\mathbf{1a}]_4$, although the Pt···Pt distances are coherent with the X-ray structure, the energy of the low-energy transition with stronger oscillator strength (S_2 391 nm) does not fit, and thus this tetramer model is not considered. With respect to the emission, the character of the lowest triplet excited state changes from ^{3}IL/^{3}MLCT character in the monomer to a mixed ^{3}MMLCT/^{3}IL in the dimer and trimer, with a higher ^{3}MMLCT character for these systems, as is seen in their spin density plots (Figure 14). In agreement with the experimental evidence, the predicted emission maxima are red-shifted in the trimer in relation to the dimer and the monomer, respectively (762 $[\mathbf{1a}]_3$, 624 $[\mathbf{1a}]_2$ *vs* 519 nm **1a**). The value of the trimer, 762 nm, can be compared to the emission of the kinetic red form **1a-CHCl$_3$-R** (662 nm), whereas the value of the dimer fits better to the orange emission of unsolvated crystals **1a** (625 nm, also pristine solid).

For **1b**, the optimized geometries of $[\mathbf{1b}]_2$ and $[\mathbf{1b}]_3$ models do not fit with the experimental X-ray diffraction structure of **1b·0.5Toluene**. $[\mathbf{1b}]_2$ and $[\mathbf{1b}]_3$ show Pt···Pt distances in their S_0 of 3.73 and 3.81 Å, respectively, longer than in the 1D chain **1b·0.5Toluene**, although shorter in the T_1 (2.87 $[\mathbf{1b}]_2$, 2.97 Å $[\mathbf{1b}]_3$). However, the computed Pt···Pt distances of the lowest-energy tetramer $[\mathbf{1b}]_4$ are 3.26 and 3.78 Å, with an orientation of the monomers in perfect agreement with the data of X-ray structural analyses of **1b·0.5Toluene**. As expected, the metallophilic Pt···Pt distances turn significantly shorter in the T_1-optimized geometry (2.94, 3.03, 3.60 Å). The S_1 transition of $[\mathbf{1b}]_4$ is derived from the HOMO → LUMO transition (95%), the HOMO being composed mainly of Pt (81%) and the LUMO of the ppy-CHO ligand (88%). This evidences the red-shifted low-energy absorptions in $[\mathbf{1b}]_4$ (527 nm) with significant MMLCT in relation to the monomer (S_1 430 nm). In relation to the emission, the predicted emission maxima of 943 nm, arising from the lowest-energy tetramer $[\mathbf{1b}]_4$ *vs* 621 nm, obtained for the monomer evidence a high ^{3}MMLCT contribution for the lowest triplet excites state, as is reflected in its spin density (Figure S44). These results confirm that the calculated red-shifted absorption and emission are induced by a packing arrangement better in dimers and trimers in **1a** and tetramers in **1b**, which improves the intermolecular interactions, leading to an increased MMLCT character.

Table 3. Calculated S_1 Vertical Excitation Energies and Emission Energy Computed in the Gas Phase (SI)

complex	state	λ (nm)	assignment	ΔE emission (T_1−S_0 opt) (nm)
1a	S_1	383	HOMO → LUMO (98%)	519
$[\mathbf{1a}]_2$	S_1	417	HOMO → LUMO (98%)	624
$[\mathbf{1a}]_3$	S_1	488	HOMO → LUMO (98%)	762
1b	S_1	430	HOMO → LUMO (97%)	621
$[\mathbf{1b}]_4$	S_1	527	HOMO → LUMO (95%)	943

CONCLUSIONS

In summary, we report the synthesis, characterization, and photophysical investigations of new phosphorescent *tert*-butylisoyanide Pt^{II} complexes with difluorophenylpyridine or formyl-functionalized phenylpyridine cyclometalated (C^N = dfppy **a**, ppy-CHO **b**) ligands: neutral, $[Pt(C^N)Cl(CNBu^t)]$ (**1**), double salts $[Pt(C^N)(CNBu^t)_2][Pt(C^N)Cl_2]$ (**2**), and cationic $[Pt(C^N)(CNBu^t)_2]ClO_4$ (**3**). A comparative study of the crystal packing of the pseudopolymorphs of **1a** (**1a**, **1a·CHCl$_3$**), **1b** (**1b**, **1b·0.5Toluene**, **1b·0.5PhF**), and **3a·0.25CH$_2$Cl$_2$** shows a great ability to be assembled by intermolecular Pt···Pt and/or $\pi\cdots\pi$ interactions in the solid state, so generating 1D columnar stackings. The structures with head-to-tail packing exhibit larger Pt···Pt distances (4.556−6.541 Å) than the structures with a head-to-head disposition (3.362−3.896 Å), which is reflected in a change of the emission from greenish or yellow to orange/red or red. We discovered that complexes **1a** and **1b** exhibit multistimuli-responsive properties, displaying vapochromism, vapoluminescence, solvatochromism, thermochromism, and mechanochromism in the solid state, which can be attributed to modulation of Pt···Pt and/or $\pi\cdots\pi$ interactions with distinct color switching from green to red. The solvates **1a·CHCl$_3$**, **1b·0.5Toluene**, and **1b·0.5PhF** contain channels running parallel to the 1D columns, occupied by the corresponding solvent, thus rationalizing the vapochromic/

https://doi.org/10.1021/acs.inorgchem.2c01400
Inorg. Chem. 2022, 61, 10898−10914

vapoluminescent/solvatochromic response of solvent-free **1a** and **1b** materials. The interactions can be established even in a polymer matrix. Thus, **1b** undergoes also supramolecular self-assembly *via* Pt···Pt and/or $\pi\cdots\pi$ interactions into a polystyrene film (PS, 10 wt %) in response to toluene vapors. Grinding the pristine solids **1a** and **1b** affects their molecular packing in the solid state, producing a color emission change to orange with the loss of crystallinity (PXRD). Theoretical simulations confirm that Pt···Pt contacts are relevant in dimer and trimer geometries in **1a** and tetramers in **1b**, especially in their T_1 states, leading to an increased MMLCT character in the solid-state aggregates.

■ ASSOCIATED CONTENT

Supporting Information

The Supporting Information is available free of charge at https://pubs.acs.org/doi/10.1021/acs.inorgchem.2c01400.

Experimental section and tables and figures giving spectroscopic, structural, photophysical, and theoretical data for compounds prepared in this paper (PDF)

Accession Codes

CCDC 2167984-2167989 contain the supporting crystallographic data for this paper. These data can be obtained free of charge *via* www.ccdc.cam.ac.uk/data_request/cif, or by mailing data_request@ccdc.cam.ac.uk, or by contacting The Cambridge Crystallographic Data Centre, 12 Union Road, Cambridge CB2 1EZ, U.K.; fax: +44 1223 336033.

■ AUTHOR INFORMATION

Corresponding Authors

Elena Lalinde − *Departamento de Química-Centro de Síntesis Química de La Rioja (CISQ), Universidad de La Rioja, 26006 Logroño, Spain;* orcid.org/0000-0001-7402-1742; Email: elena.lalinde@unirioja.es

M. Teresa Moreno − *Departamento de Química-Centro de Síntesis Química de La Rioja (CISQ), Universidad de La Rioja, 26006 Logroño, Spain;* orcid.org/0000-0002-7744-9805; Email: teresa.moreno@unirioja.es

Author

Mónica Martínez-Junquera − *Departamento de Química-Centro de Síntesis Química de La Rioja (CISQ), Universidad de La Rioja, 26006 Logroño, Spain*

Complete contact information is available at: https://pubs.acs.org/10.1021/acs.inorgchem.2c01400

Notes

The authors declare no competing financial interest.

■ ACKNOWLEDGMENTS

This work was supported by the Spanish Ministerio de Ciencia e Innovación (Project PID2019-109742GB-I00) funded by MCIN/AIE/10.13039/501100011033 and by "ERDF A way of making Europe", by the "European Union". M.M.-J. is grateful to UR for a Ph.D. grant. The authors acknowledge the support of "Avanzare Innovación Tecnológica S.L." for PXRD analysis.

■ REFERENCES

(1) Soto, M. A.; Kandel, R.; MacLachlan, M. J. Chromic Platinum Complexes Containing Multidentate Ligands. *Eur. J. Inorg. Chem.* **2021**, *2021*, 894−906.

(2) (a) Zheng, Q.; Borsley, S.; Tu, T.; Cockroft, S. L. Reversible stimuli-responsive chromism of a cyclometallated platinum(II) complex. *Chem. Commun.* **2020**, *56*, 14705−14708. (b) Soto, M. A.; Carta, V.; Andrews, R. J.; Chaudhry, M. T.; MacLachlan, M. J. Structural Elucidation of Selective Solvatochromism in a Responsive-at-Metal Cyclometalated Platinum(II) Complex. *Angew. Chem., Int. Ed.* **2020**, *59*, 10348−10352. (c) Chen, J.; Ao, L.; Wei, C.; Wang, C.; Wang, F. Self-assembly of platinum(II) 6-phenyl-2,2′-bipyridine complexes with solvato- and iono-chromic phenomena. *Chem. Commun.* **2019**, *55*, 229−232. (d) Liao, K.-Y.; Hsu, C.-W.; Chi, Y.; Hsu, M.-K.; Wu, S.-W.; Chang, C.-H.; Liu, S.-H.; Lee, G.-H.; Chou, P.-T.; Hu, Y.; Robertson, N. Pt(II) Metal Complexes Tailored with a Newly Designed Spiro-Arranged Tetradentate Ligand; Harnessing of Charge-Transfer Phosphorescence and Fabrication of Sky Blue and White OLEDs. *Inorg. Chem.* **2015**, *54*, 4029−4038.

(3) (a) Cuerva, C.; Campo, J. A.; Cano, M.; Lodeiro, C. Multi-Stimuli-Responsive Properties of Aggregation-Enhanced Emission-Active Unsymmetrical Pt^{II} Metallomesogens through Self-Assembly. *Chem.—Eur. J.* **2019**, *25*, 12046−12051. (b) Kobayashi, A.; Imada, S.-I.; Shigeta, Y.; Nagao, Y.; Yoshida, M.; Kato, M. Vapochromic luminescent proton conductors: switchable vapochromism and proton conduction of luminescent Pt(II) complexes with proton-exchangeable sites. *J. Mater. Chem. C* **2019**, *7*, 14923−14931. (c) Kobayashi, A.; Yamamoto, N.; Shigeta, Y.; Yoshida, M.; Kato, M. Two-way vapochromism of a luminescent platinum(II) complex with phosphonic-acid-functionalized bipyridine ligand. *Dalton Trans.* **2018**, *47*, 1548−1556. (d) Ohno, K.; Kusano, Y.; Kaizaki, S.; Nagasawa, A.; Fujihara, T. Chromism of Tartrate-Bridged Clamshell-like Platinum-(II) Complex: Intramolecular Pt−Pt Interaction-Induced Luminescence Vapochromism and Intermolecular Interactions-Triggered Thermochromism. *Inorg. Chem.* **2018**, *57*, 14159−14169.

(4) (a) Ma, Y.; Chen, K.; Lu, J.; Shen, J.; Ma, C.; Liu, S.; Zhao, Q.; Wong, W.-Y. Phosphorescent Soft Salt Based on Platinum(II) Complexes: Photophysics, Self-Assembly, Thermochromism, and Anti-counterfeiting Application. *Inorg. Chem.* **2021**, *60*, 7510−7518. (b) Liu, L.; Wang, X.; Wang, N.; Peng, T.; Wang, S. Bright, Multi-responsive, Sky-Blue Platinum(II) Phosphors Based on a Tetradentate Chelating Framework. *Angew. Chem., Int. Ed.* **2017**, *56*, 9160−9164.

(5) (a) Zhang, H.-H.; Wu, S.-X.; Wang, Y.-Q.; Xie, T.-G.; Sun, S.-S.; Liu, Y.-L.; Han, L.-Z.; Zhang, X.-P.; Shi, Z.-F. Mechanochromic luminescent property and anti-counterfeiting application of AIE-active cyclometalated platinum(II) complexes featuring a fused five-six-membered metallacycle. *Dyes Pigm.* **2022**, *197*, No. 109857. (b) Yang, Q.-Y.; Zhang, H.-H.; Qi, X.-W.; Sun, S.-S.; Zhang, D.-S.; Han, L.-Z.; Zhang, X.-P.; Shi, Z.-F. Mechanochromic luminescence properties of fluoro-substituted pinene-containing cyclometalated platinum(II) complexes with multiple triplet excited states. *Dalton Trans.* **2021**, *50*, 8938−8946. (c) Ai, Y.; Li, Y.; Chan, M. H.-Y.; Xiao, G.; Zou, B.; Yam, V. W.-W. Realization of Distinct Mechano- and Piezochromic Behaviors via Alkoxy Chain Length-Modulated Phosphorescent Properties and Multidimensional Self-Assembly Structures of Dinuclear Platinum(II) Complexes. *J. Am. Chem. Soc.* **2021**, *143*, 10659−10667. (d) Norton, A. E.; Abdolmaleki, M. K.; Liang, J.; Sharma, M.; Golsby, R.; Zoller, A.; Krause, J. A.; Connick, W. B.; Chatterjee, S. Phase transformation induced mechanochromism in a platinum salt: a tale of two polymorphs. *Chem. Commun.* **2020**, *56*, 10175−10178.

(6) (a) Chung, C. Y.-S.; Li, S. P.-Y.; Louie, M.-W.; Lo, K. K.-W.; Yam, V. W.-W. Induced self-assembly and disassembly of water-soluble alkynylplatinum(II) terpyridyl complexes with "switchable" near-infrared (NIR) emission modulated by metal−metal interactions over physiological pH: demonstration of pH-responsive NIR luminescent probes in cell-imaging studies. *Chem. Sci.* **2013**, *4*, 2453−2462. (b) Leung, S. Y.-L.; Yam, V. W.-W. Hierarchical helices of helices directed by Pt···Pt and $\pi-\pi$ stacking interactions: reciprocal association of multiple helices of dinuclear alkynylplatinum(II) complex with luminescence enhancement behavior. *Chem. Sci.* **2013**, *4*, 4228−4234. (c) Chung, C. Y.-S.; Chan, K. H.-Y.; Yam, V. W.-W. "Proof-of-principle" concept for label-free detection of glucose and α-glucosidase activity through the electrostatic assembly of alkynylplatinum(II) terpyridyl complexes. *Chem. Commun.* **2011**, *47*, 2000−2002.

(7) (a) Yoshida, M.; Kato, M. Regulation of metal−metal interactions and chromic phenomena of multi-decker platinum complexes having π-systems. *Coord. Chem. Rev.* **2018**, *355*, 101−115. (b) Kobayashi, A.; Kato, M. Vapochromic Platinum(II) Complexes: Crystal Engineering toward Intelligent Sensing Devices. *Eur. J. Inorg. Chem.* **2014**, 4469−4483. (c) Wenger, O. S. Vapochromism in Organometallic and Coordination Complexes: Chemical Sensors for Volatile Organic Compounds. *Chem. Rev.* **2013**, *113*, 3686−3733. (d) Zhang, X.; Chi, Z.; Zhang, Y.; Liu, S.; Xu, J. Recent advances in mechanochromic luminescent metal complexes. *J. Mater. Chem. C* **2013**, *1*, 3376−3390. (e) Zhang, X.; Li, B.; Chen, Z. H.; Chen, Z. N. Luminescence vapochromism in solid materials based on metal complexes for detection of volatile organic compounds (VOCs). *J. Mater. Chem.* **2012**, *22*, 11427−11441. (f) Xue, P.; Ding, J.; Wang, P.; Lu, R. Recent progress in the mechanochromism of phosphorescent organic molecules and metal complexes. *J. Mater. Chem. C* **2016**, *4*, 6688−6706. (g) Yam, V. W.-W.; Au, V. K.-M.; Leung, S. Y.-L. Light-Emitting Self-Assembled Materials Based on d^8 and d^{10} Transition Metal Complexes. *Chem. Rev.* **2015**, *115*, 7589−7728. (h) Li, B.; Fan, H.-T.; Zang, S.-Q.; Li, H.-Y.; Wang, L.-Y. Metal-containing crystalline luminescent thermochromic materials. *Coord. Chem. Rev.* **2018**, *377*, 307−329. (i) Yoshida, M.; Kato, M. Cation-controlled luminescence behavior of anionic cyclometalated platinum(II) complexes. *Coord. Chem. Rev.* **2020**, *408*, No. 213194.

(8) (a) Zhang, X.; Wang, J.-Y.; Ni, J.; Zhang, L.-Y.; Chen, Z.-N. Vapochromic and Mechanochromic Phosphorescence Materials Based on a Platinum(II) Complex with 4-Trifluoromethylphenylacetylide. *Inorg. Chem.* **2012**, *51*, 5569−5579. (b) Ku, H.-Y.; Tong, B.; Chi, Y.; Kao, H.-C.; Yeh, C.-C.; Chang, C.-H.; Lee, G.-H. Luminescent Pt(II) complexes bearing dual isoquinolinyl pyrazolates: fundamentals and applications. *Dalton Trans.* **2015**, *44*, 8552−8563. (c) Su, M.; Liu, S.; Zhang, J.; Meng, C.; Ni, J. The triple-stimuli-responsive luminescence switching properties and application of a square-planar platinum(II) complex. *Dyes Pigm.* **2022**, *200*, No. 110139.

(9) (a) Puttock, E. V.; Walden, M. T.; Williams, J. A. G. The luminescence properties of multinuclear platinum complexes. *Coord. Chem. Rev.* **2018**, *367*, 127−162. (b) Aliprandi, A.; Genovese, D.; Mauro, M.; Cola, L. D. Recent Advances in Phosphorescent Pt(II) Complexes Featuring Metallophilic Interactions: Properties and Applications. *Chem. Lett.* **2015**, *44*, 1152−1169. (c) Gray, H. B.; Záliš, S.; Vlček, A. Electronic structures and photophysics of d^8-d^8 complexes. *Coord. Chem. Rev.* **2017**, *345*, 297−317. (d) Kim, D.; Brédas, J.-L. Triplet Excimer Formation in Platinum-Based Phosphors: A Theoretical Study of the Roles of Pt−Pt Bimetallic Interactions and Interligand π−π Interactions. *J. Am. Chem. Soc.* **2009**, *131*, 11371−11380.

(10) (a) Nakagaki, M.; Aono, S.; Kato, M.; Sakaki, S. Delocalization of the Excited State and Emission Spectrum of the Platinum(II) Bipyridine Complex in Crystal: Periodic QM/MM Study. *J. Phys. Chem. C* **2020**, *124*, 10453−10461. (b) Park, G.; Kim, H.; Yang, H.; Park, K. R.; Song, I.; Oh, J. H.; Kim, C.; You, Y. Amplified circularly polarized phosphorescence from co-assemblies of platinum(II) complexes. *Chem. Sci.* **2019**, *10*, 1294−1301.

(11) (a) Genovese, D.; Aliprandi, A.; Prasetyanto, E. A.; Mauro, M.; Hirtz, M.; Fuchs, H.; Fujita, Y.; Uji-I, H.; Lebedkin, S.; Kappes, M.; De Cola, L. Mechano- and Photochromism from Bulk to Nanoscale: Data Storage on Individual Self-Assembled Ribbons. *Adv. Funct. Mater.,* **2016**, *26*, 5271−5278. (b) Tan, G.; Chen, S.; Siu, C.-H.; Langlois, A.; Qiu, Y.; Fan, H.; Ho, C.-L.; Harvey, P. D.; Lo, Y. H.; Liu, L.; Wong, W.-Y. Platinum(II) cyclometallates featuring broad emission bands and their applications in color-tunable OLEDs and high color-rendering WOLEDs. *J. Mater. Chem. C* **2016**, *4*, 6016−6026. (c) Huang, L.-M.; Tu, G.-M.; Chi, Y.; Hung, W.-Y.; Song, Y.-C.; Tseng, M.-R.; Chou, P.-T.; Lee, G.-H.; Wong, K.-T.; Cheng, S.-H.; Tsai, W.-S. Mechanoluminescent and efficient white OLEDs for Pt(II) phosphors bearing spatially encumbered pyridinyl pyrazolate chelates. *J. Mater. Chem. C* **2013**, *1*, 7582−7592. (d) Rossi, E.; Murphy, L.; Brothwood, P. L.; Colombo, A.; Dragonetti, C.; Roberto, D.; Ugo, R.; Cocchi, M.; Williams, J. A. G. Cyclometallated platinum(II) complexes of 1,3-di(2-pyridyl)benzenes: tuning excimer emission from red to near-infrared for NIR-OLEDs. *J. Mater. Chem.* **2011**, *21*, 15501−15510. (e) Chen, W.-C.; Sukpattanacharoen, C.; Chan, W.-H.; Huang, C.-C.; Hsu, H.-F.; Shen, D.; Hung, W.-Y.; Kungwan, N.; Escudero, D.; Lee, C.-S.; Chi, Y. Modulation of Solid-State Aggregation of Square-Planar Pt(II) Based Emitters: Enabling Highly Efficient Deep-Red/Near Infrared Electroluminescence. *Adv. Funct. Mater.* **2020**, *30*, No. 2002494.

(12) (a) Inoue, R.; Naota, T.; Ehara, M. Origin of the Aggregation-Induced Phosphorescence of Platinum(II) Complexes: The Role of Metal−Metal Interactions on Emission Decay in the Crystalline State. *Chem.—Asian J.* **2021**, *16*, 3129−3140. (b) Rossi, E.; Colombo, A.; Dragonetti, C.; Roberto, D.; Ugo, R.; Valore, A.; Falciola, L.; Brulatti, P.; Cocchi, M.; Williams, J. A. G. Novel N^C^N-cyclometallated platinum complexes with acetylide co-ligands as efficient phosphors for OLEDs. *J. Mater. Chem.* **2012**, *22*, 10650−10655. (c) Perez, M. D.; Djurovich, P. I.; Hassan, A.; Cheng, G. Y.; Stewart, T. J.; Aznavour, K.; Bau, R.; Thompson, M. E. Exciplex quenching of a luminescent cyclometallated platinum complex by extremely poor Lewis bases. *Chem. Commun.* **2009**, 4215−4217.

(13) Pyykkö, P. Strong Closed-Shell Interactions in Inorganic Chemistry. *Chem. Rev.* **1997**, *97*, 597−636.

(14) (a) Díez, A.; Forniés, J.; Larraz, C.; Lalinde, E.; López, J. A.; Martín, A.; Moreno, M. T.; Sicilia, V. Structural and Luminescence Studies on π···π and Pt···Pt Interactions in Mixed Chloro-Isocyanide Cyclometalated Platinum(II) Complexes. *Inorg. Chem.* **2010**, *49*, 3239−3251. (b) Sluch, I. M.; Miranda, A. J.; Elbjeirami, O.; Omary, M. A.; Slaughter, L. M. Interplay of Metallophilic Interactions, π−π Stacking, and Ligand Substituent Effects in the Structures and Luminescence Properties of Neutral Pt^{II} and Pd^{II} Aryl Isocyanide Complexes. *Inorg. Chem.* **2012**, *51*, 10728−10746. (c) Cho, Y.-J.; Kim, S.-Y.; Son, H.-J.; Cho, D. W.; Kang, S. O. Steric effect on excimer formation in planar Pt(II) complexes. *Phys. Chem. Chem. Phys.* **2017**, *19*, 5486−5494.

(15) Koshevoy, I. O.; Krause, M.; Klein, A. Non-covalent intramolecular interactions through ligand-design promoting efficient photoluminescence from transition metal complexes. *Coord. Chem. Rev.* **2020**, *405*, No. 213094.

(16) (a) Bryant, M. J.; Skelton, J. M.; Hatcher, L. E.; Stubbs, C.; Madrid, E.; Pallipurath, A. R.; Thomas, L. H.; Woodall, C. H.; Christensen, J.; Fuertes, S.; Robinson, T. P.; Beavers, C. M.; Teat, S. J.; Warren, M. R.; Pradaux-Caggiano, F.; Walsh, A.; Marken, F.; Carbery, D. R.; Parker, S. C.; McKeown, N. B.; Malpass-Evans, R.; Carta, M.; Raithby, P. R. A rapidly-reversible absorptive and emissive vapochromic Pt(II) pincer-based chemical sensor. *Nat. Commun.* **2017**, *8*, No. 1800. (b) Forniés, J.; Fuertes, S.; López, J. A.; Martín, A.; Sicilia, V. New Water Soluble and Luminescent Platinum(II) Compounds, Vapochromic Behavior of $[K(H_2O)][Pt(bzq)(CN)_2]$. New Examples of the Influence of the Counterion on the Photophysical Properties of d^8 Square-Planar Complexes. *Inorg. Chem.* **2008**, *47*, 7166−7176. (c) Chan, M. H.-Y.; Wong, H.-L.; Yam, V. W.-W. Synthesis and Photochromic Studies of Dithienylethene-Containing Cyclometalated Alkynylplatinum(II) 1,3-Bis(N-alkylbenzimidazol-2′-yl)benzene Complexes. *Inorg. Chem.* **2016**, *55*, 5570−5577. (d) Lien, C.-Y.; Hsu, Y.-F.; Liu, Y.-H.; Peng, S.-M.; Shinmyozu, T.; Yang, J.-S. Steric Engineering of Cyclometalated Pt(II) Complexes toward High-Contrast Monomer−Excimer-Based Mechanochromic and Vapochromic Luminescence. *Inorg. Chem.* **2020**, *59*, 11584−11594. (e) Belviso, B. D.; Marin, F.; Fuertes, S.; Sicilia, V.; Rizzi, R.; Ciriaco, F.; Cappuccino, C.; Dooryhee, E.; Falcicchio, A.; Maini, L.; Altomare, A.; Caliandro, R. Structural Insights into the Vapochromic Behavior of Pt- and Pd-Based Compounds. *Inorg. Chem.* **2021**, *60*, 6349−6366.

(17) (a) Sun, Y.; Ye, K.; Zhang, H.; Zhang, J.; Zhao, L.; Li, B.; Yang, G.; Yang, B.; Wang, Y.; Lai, S.-W.; Che, C.-M. Luminescent One-Dimensional Nanoscale Materials with Pt^{II}···Pt^{II} Interactions. *Angew. Chem., Int. Ed.* **2006**, *45*, 5610−5613. (b) Zhang, Y.; Zhang, H.; Mu, X.; Lai, S.-W.; Xu, B.; Tian, W.; Wang, Y.; Che, C.-M. Photo- and vapor-responsive conducting microwires based on Pt···Pt interactions. *Chem. Commun.* **2010**, *46*, 7727−7729. (c) Janzen, D. E.; Mann, K. R. Heteroleptic platinum(II) isocyanide complexes: convenient synthetic

https://doi.org/10.1021/acs.inorgchem.2c01400
Inorg. Chem. 2022, 61, 10898−10914

access, polymorphs, and vapoluminescence. *Dalton Trans.* **2015**, *44*, 4223−4237. (d) Kuwabara, J.; Yamaguchi, K.; Yamawaki, K.; Yasuda, T.; Nishimura, Y.; Kanbara, T. Modulation of the Emission Mode of a Pt(II) Complex via Intermolecular Interactions. *Inorg. Chem.* **2017**, *56*, 8726−8729.

(18) Katkova, S. A.; Luzyanin, K. V.; Novikov, A. S.; Kinzhalov, M. A. Modulation of luminescence properties for [cyclometalated]-Pt^{II}(isocyanide) complexes upon co-crystallisation with halosubstituted perfluorinated arenes. *New J. Chem.* **2021**, *45*, 2948−2952.

(19) (a) Martínez-Junquera, M.; Lara, R.; Lalinde, E.; Moreno, M. T. Isomerism, aggregation-induced emission and mechanochromism of isocyanide cycloplatinated(II) complexes. *J. Mater. Chem. C* **2020**, *8*, 7221−7233. (b) Chen, Y.; Lu, W.; Che, C.-M. Luminescent Pincer-Type Cyclometalated Platinum(II) Complexes with Auxiliary Isocyanide Ligands: Phase-Transfer Preparation, Solvatomorphism, and Self-Aggregation. *Organometallics* **2013**, *32*, 350−353. (c) Forniés, J.; Sicilia, V.; Larraz, C.; Camerano, J. A.; Martín, A.; Casas, J. M.; Tsipis, A. C. One-Pot and Step-by-Step N-Assisted CPh−H Activation in 2-(4-Bromophenyl)imidazol[1,2-*a*]pyridine: Synthesis of a New C,N-Cyclometalated Compound $[\{Pt(C\wedge N)(\mu\text{-}Cl)\}_2]$ as Precursor of Luminescent Platinum(II) Compounds. *Organometallics* **2010**, *29*, 1396−1405. (d) Lu, W.; Chan, M. C. W.; Cheung, K.-K.; Che, C.-M. $\pi-\pi$ Interactions in Organometallic Systems. Crystal Structures and Spectroscopic Properties of Luminescent Mono-, Bi-, and Trinuclear Trans-cyclometalated Platinum(II) Complexes Derived from 2,6-Diphenylpyridine. *Organometallics* **2001**, *20*, 2477−2486. (e) Paziresh, S.; Babadi Aghakhanpour, R.; Fuertes, S.; Sicilia, V.; Niroomand Hosseini, F.; Nabavizadeh, S. M. A double rollover cycloplatinated(II) skeleton: a versatile platform for tuning emission by chelating and non-chelating ancillary ligand systems. *Dalton Trans.* **2019**, *48*, 5713−5724. (f) Lai, S.-W.; Lam, H.-W.; Lu, W.; Cheung, K.-K.; Che, C.-M. Observation of Low-Energy Metal−Metal-to-Ligand Charge Transfer Absorption and Emission: Electronic Spectroscopy of Cyclometalated Platinum(II) Complexes with Isocyanide Ligands. *Organometallics* **2002**, *21*, 226−234.

(20) Cho, J.-Y.; Suponitsky, K. Y.; Li, J.; Timofeeva, T. V.; Barlow, S.; Marder, S. R. Cyclometalated platinum complexes: High-yield synthesis, characterization, and a crystal structure. *J. Organomet. Chem.* **2005**, *690*, 4090−4093.

(21) Katkova, S. A.; Eliseev, I. I.; Mikherdov, A. S.; Sokolova, E. V.; Starova, G. L.; Kinzhalov, M. A. Cyclometalated Platinum(II) Complexes with Nitrile and Isocyanide Ligands: Synthesis, Structure, and Photophysical Properties. *Russ. J. Gen. Chem.* **2021**, *91*, 393−400.

(22) Forniés, J.; Fuertes, S.; Larraz, C.; Martín, A.; Sicilia, V.; Tsipis, A. C. Synthesis and Characterization of the Double Salts $[Pt(bzq)(CNR)_2][Pt(bzq)(CN)_2]$ with Significant Pt···Pt and $\pi\cdots\pi$ Interactions. Mechanistic Insights into the Ligand Exchange Process from Joint Experimental and DFT Study. *Organometallics* **2012**, *31*, 2729−2740.

(23) Connick, W. B.; Marsh, R. E.; Schaefer, W. P.; Gray, H. B. Linear-Chain Structures of Platinum(II) Diimine Complexes. *Inorg. Chem.* **1997**, *36*, 913−922.

(24) Macrae, C. F.; Sovago, I.; Cottrell, S. J.; Galek, P. T. A.; McCabe, P.; Pidcock, E.; Platings, M.; Shields, G. P.; Stevens, J. S.; Towler, M.; Wood, P. A. Mercury 4.0: from visualization to analysis, design and prediction. *J. Appl. Crystallogr.* **2020**, *53*, 226−235.

(25) Baldo, M. A.; Adachi, C.; Forrest, S. R. Transient analysis of organic electrophosphorescence. II. Transient analysis of triplet-triplet annihilation. *Phys. Rev. B* **2000**, *62*, 10967−10977.

(26) Sutton, G. D.; Olumba, M. E.; Nguyen, Y. H.; Teets, T. S. The diverse functions of isocyanides in phosphorescent metal complexes. *Dalton Trans.* **2021**, *50*, 17851−17863.

(27) Cuerva, C.; Campo, J. A.; Cano, M.; Caño-García, M.; Otón, J. M.; Lodeiro, C. Aggregation-induced emission enhancement (AIEE)-active Pt(II) metallomesogens as dyes sensitive to Hg^{2+} and dopant agents to develop stimuli-responsive luminescent polymer materials. *Dyes Pigm.* **2020**, *175*, No. 108098.

https://doi.org/10.1021/acs.inorgchem.2c01400
Inorg. Chem. 2022, 61, 10898−10914